LBNL-51777

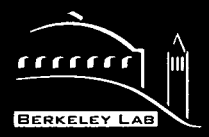

ERNEST ORLANDO LAWRENCE
BERKELEY NATIONAL LABORATORY

Chemical Dynamics Applications of Semiclassical Methods

Jianhua Xing

Chemical Sciences Division

November 2002

Ph.D. Thesis

LBNL-51777

DISCLAIMER

LBNL-51777

Chemical Dynamics Applications of Semiclassical Methods

Jianhua Xing

Ph.D. Thesis

Department of Chemistry
University of California, Berkeley

and

Chemical Science Division
Ernest Orlando Lawrence Berkeley National Laboratory
University of California
Berkeley, CA 94720

November 2002

This work was supported by the Office of Naval Research, Grant Number N00014-01-1-0236 and by the Director, Office of Science, Office of Basic Energy Sciences, Chemical Sciences, Geosciences, and Biosciences Division, U. S. Department of Energy under Contract Number DE-AC03-76SF00098.

Chemical Dynamics Applications of Semiclassical Methods

by

Jianhua Xing

B. S. (Peking University) 1996

M. S. (University of Minnesota) 1998

A dissertation submitted in partial satisfaction of the

requirements for the degree of

Doctor of Philosophy

in

Chemistry

in the

GRADUATE DIVISION

of the

UNIVERSITY of CALIFORNIA, BERKELEY

Committee in Charge:

Professor William H. Miller, Chair

Professor Martin Head-Gordon

Professor Eugene Commins

Fall 2002

Chemical Dynamics Applications of Semicalssical Methods

by

Jianhua Xing

Abstract

Chemical Dynamics Applications of Semiclassical Methods

by

Jianhua Xing

Doctor of Philosophy in Chemistry

University of California, Berkeley

Professor William H. Miller, Chair

Quantum mechanics is the ultimate theory in studying chemical dynamics. However, in practice full quantum calculations are limited to small systems. Semiclassical initial-value-representation (SC-IVR) method is a potential alternative for including quantum effects into classical trajectory calculations. This work presents efforts on applying SC-IVR method and approximations onto various chemical dynamics problems.

A nonadiabatic process involves nuclei motions on several potential energy surfaces. The McCurdy-Meyer-Miller hamiltonian maps the discrete (multi-surface) system into a continuous system, which is ready for SC-IVR applications. A three-state model was tested with the SC-IVR method and its linearized approximations. The calculated absorption spectra, auto-correlation functions, and branch populations agree well with exact quantum results.

A novel application of the McCurdy-Meyer-Miller hamiltonian for describing tunneling was discussed.

Calculating thermal rate constants of chemical reactions is a central task in theoretical chemical dynamics. The thermal rate constants were calculated with the Miller-Schwartz-Tromp correlation function formalism. The calculation involves imaginary and real time propagator, which were calculated with path-integral (PI) and SC-IVR, respectively. The focus of the study was on practical

ways of implementing the PI and various versions of the semiclassical method: the full double space SC-IVR , the forward-backward (FB), and the linearized SC-IVR methods. Tests were performed on a system with an Eckhart barrier bilinearly coupled to harmonic baths, and encouraging results were obtained.

To my family

Contents

List of Figures

List of Tables

Acknowledgements

First, I would like to thank my advisor, Professor Miller for taking me into his group. As a world famous theoretical chemist, Bill provided insightful guidance during my Ph. D. period. He also gave me great freedom in exploring various projects. From his quantum mechanics and kinetics classes, I learnt to think the theories from a chemist's point of view. He also gave me a lot of opportunities to practice teaching in his quantum mechanics class.

Mrs. Cheryn Gliebe, as a manager of the Miller group, is always supportive. It is a pleasure to chat with her after hours of focusing on science. Please take my cordly thanks, Cheryn.

I would like to thank the entire Miller group. As a small "united nations", we have the opportunities to share different cultures as well understandings of science. I would particularly like to thank to those Miller group members with whom I have close contacts: Dr. Haobin Wang and Dr. Michael Thoss patiently explained details and tricks of semiclassical calculations when I jointed group, then also gave me valuable suggestions on some of my projects; Dr. Eduardo Coronado and Dr. Ricard Gelabert were my officemates and collaborators; Dr. Takeshi Yamamoto and Dr. Mark Brewer had inspiring discussions with me on rate constant calculations.

My early years at Berkeley also include taking wonderful courses given by Professor Dung-Hai Lee, Professor David Chandler, Professor Eugene Commins, and Professor Bill Miller.

I would like to thank my wife for her support and encouragement throughout my Ph. D. period, especially when I was in depression. My family gave me lasting support throughout my student life, especially my parents helped us taking care of my daughter born on last September 11th.

This work was supported by the Office of Naval Research, Grant Number N00014-01-1-0236 and by the Director, Office of Science, Office of Basic Energy Sciences, Chemical Sciences, Geosciences, and Biosciences Division, U. S. Department of Energy under Contract Number DE-AC03-76SF00098. We also

acknowledge a generous allocation of supercomputing time from the National Energy Research Scientific Computing Center (NERSC).

Chapter 1

Semiclassical Basics

1.1 Introduction

Within the energy range of chemical reactions, quantum mechanics is the *final* theory. The last several decades have seen tremendous progresses in molecular electronic structure calculations. Nowadays, many user-friendly computer packages of quantum chemistry exist for non-experts, and quantum chemistry calculations are routine tasks to most modern chemists. In contrast, theoretical studies of chemical dynamics (or generally, about nuclei motions) are far behind. While molecular beam experiments have demonstrated the close agreement between quantum mechanical calculations and experimental results for small systems, currently full quantum mechanical calculations are restricted to three or four atom systems. The difficulty is apparent: the wavefunction of a system needs to be expanded on a basis set, and the number of basis functions grows exponentially with the number of degrees of freedom. The situation is quite like a "full CI" calculation in the electronic structure theories. One may be surprised why nuclei motions are harder to study than electronic motions, while electrons are supposed to be more quantum behaved than nuclei do. One reason is that the electronic hamiltonian can always be decomposed into one-particle and two-particle operators, and the nuclei hamiltonian (obtained by integrating out the electronic degrees of freedom, e.g. the Born-Oppenheimer approximation) can not

in general. Within currrent computer technology, approximate methodologies for chemical dynamic studies have been developed. Some of them are in parallel to the electronic theory, for example, the multi-configuration-time-dependent-hartree method[1].

The semiclassical (SC) method is an asymptotic type approximation. Derivations of a SC formula usually start with a series expansion of the classical action over $\hbar$, and usually the series is cut off at the first order of $\hbar$. For chemical applications, which are composed of nuclei much heavier than electrons, this approximation is sufficient in most situations. The first example of semiclassical theory is the Wentzel-Krammers-Brillouin (WKB) approximation and its generalizations[2]. The WKB approximations can be used to derive the "corrected" Bohr-Sommerfeld[3] and Einstein-Brillouin-Keller[4] quantization relations. The WKB approximation is an energy-domain theory. For dynamical processes, the propagator, $\exp(-i\hat{H}t/\hbar)$, is more useful. The form of semiclassical propagator was first proposed by Van Vleck[5], then was derived through a stationary phase approximation of the Feynman's path integral representation of the propagator by Gutzwiller and others[6–9]. The Van Vleck propagator reads,

$$\begin{aligned}\langle \mathbf{q_2}|exp(-i\hat{H}t/\hbar)|\mathbf{q_1}\rangle &= \sum_j \left| det\left(-\frac{\partial^2 S_j(\mathbf{q_2},\mathbf{q_1})}{\partial \mathbf{q_2}\partial \mathbf{q_1}}\right)\right|^{1/2} (2\pi i\hbar)^{-F/2} \\ &\quad \exp[iS_j(\mathbf{q_2},\mathbf{q_1},t)/\hbar - i\pi\nu_j/2], \end{aligned} \tag{1.1}$$

where F is the number of degrees of freedom, and the classical action S and the Maslov index ν will be defined in the next section. Physically, the Van Vleck formula expresses the propagator as a sum of all the classical trajectories starting from $\mathbf{q_1}$ and arriving at $\mathbf{q_2}$ at time t and the path integral paths infinitesmally close to these classical paths. Finding the classical paths is a boundary condition problem, and is numerically awkward. One can only use the "shooting" method, which is not convenient for multidimensional problems. Miller, in 1970, suggested the initial value representation (IVR)[10] . He noticed that integration over both of the two end points was needed in most applications. One may do a variable

transform from $\mathbf{q_2}$ to $\mathbf{p_1}$, the intial momentum, and reachs,

$$\int d\mathbf{q_2} \sum_j \rightarrow \int d\mathbf{p_1} \left| det \left(\frac{\partial \mathbf{q_2}}{\partial \mathbf{p_1}} \right) \right|. \tag{1.2}$$

Early works on semiclassical dynamics result in the "instanton" theory of tunneling[11], which becomes a popular tool in both chemistry and physics.

In the last decade, there is a rebirth of interest in the semiclassical method[12–24]. Currently most of the works adopt a coherent-state semiclassical propagator proposed by Herman and Kluk[12]. Unlike the Van Vleck propagator, the Herman-Kluk propagator treats the momentum and coordinate on an equal foot, which is attractive both theoretically and practically. Many studies have demonstrated the accuracy and practibility of the Herman-Kluk propagator. Several approximate semiclassical theories were also developed, such as the forward-backward (FB)[28–30], the generalized forward-backward (GFB)[31], and the linearized SC-IVR[25,26]. In the following section, the basic formula and methods used in modern research on semiclassical dynamics will be discussed.

1.2 Theory

Here we discuss SC-IVR in the coherent-state representation, the more familiar coordinate (momentum) representation can be obtained as a limiting case. For the current discussion, one only needs to know that the coherent-state representation is a mixed representation of coordinate and momentum. A coherent state is given by

$$\langle \mathbf{x}|\mathbf{pq}\rangle = \left(\frac{|\gamma|}{\pi^F}\right)^{1/4} \exp\left[-\frac{1}{2}(\mathbf{x}-\mathbf{q})^T \cdot \gamma \cdot (\mathbf{x}-\mathbf{q}) + \frac{i}{\hbar}\mathbf{p}^T \cdot (\mathbf{x}-\mathbf{q})\right], \tag{1.3}$$

in the coordinate representation, and

$$\langle \mathbf{p}|\mathbf{pq}\rangle = \left(\frac{1}{|\gamma|\pi^F}\right)^{1/4} \exp\left[-\frac{1}{2}(\mathbf{x}-\mathbf{q})^T \cdot \gamma \cdot (\mathbf{x}-\mathbf{q}) + \frac{i}{\hbar}\mathbf{p}^T \cdot (\mathbf{x}-\mathbf{q})\right] \tag{1.4}$$

in the momentum representation, where γ is a constant matrix. Therefore, a coherent-state wavepacket gives gaussian distribution for both coordinate and

momentum. The coherent-state basis set is overcomplete, and the closure relation is given by,

$$\int d\mathbf{p} \int d\mathbf{q} \, |\mathbf{p}, \mathbf{q}; \gamma\rangle\langle \mathbf{p}, \mathbf{q}, \gamma| = 1 \tag{1.5}$$

A semiclassical approximation for the flux correlation function can be obtained by using the IVR for the time evolution operator $e^{-i\hat{H}t/\hbar}$, and the Herman-Kluk (HK)[12] or coherent state version of which is given by:

$$e^{-i\hat{H}t/\hbar} \approx (2\pi\hbar)^{-F} \int d\mathbf{p_0} \int d\mathbf{q_0} \, C_t(\mathbf{p_0}, \mathbf{q_0}) e^{iS_t(\mathbf{p_0},\mathbf{q_0})/\hbar} |\mathbf{p_t q_t}\rangle\langle \mathbf{p_0 q_0}|, \tag{1.6}$$

where F is the number of degrees of freedom, $(\mathbf{p}_0, \mathbf{q}_0)$ are the initial momenta and coordinates for a classical trajectory, $\mathbf{p}_t \equiv \mathbf{p}_t(\mathbf{p}_0, \mathbf{q}_0)$ and $\mathbf{q}_t \equiv \mathbf{q}_t(\mathbf{p}_0, \mathbf{q}_0)$ are the values at time t that result from this trajectory, and S_t is the classical action integral along it,

$$S_t(\mathbf{p}_0, \mathbf{q}_0) = \int_0^t d\tau \, \mathbf{p}_\tau \dot{\mathbf{q}}_\tau - H(\mathbf{p}_\tau, \mathbf{q}_\tau). \tag{1.7}$$

where the HK "pre-factor" $C_t(\mathbf{p}_0, \mathbf{q}_0)$ in Eq. 1.6 is given by[14]

$$C_t(\mathbf{p_0}, \mathbf{q_0}) = \left| \frac{1}{2} \left(\gamma^{\frac{1}{2}} \mathbf{M_{qq}} \gamma^{-\frac{1}{2}} + \gamma^{-\frac{1}{2}} \mathbf{M_{pp}} \gamma^{\frac{1}{2}} - i\hbar\gamma^{\frac{1}{2}} \mathbf{M_{qp}} \gamma^{\frac{1}{2}} + \frac{i}{\hbar} \gamma^{-\frac{1}{2}} \mathbf{M_{pq}} \gamma^{-\frac{1}{2}} \right) \right|^{1/2}, \tag{1.8}$$

where $\mathbf{M_{qq}}$, etc., are elements of the monodromy matrix[27]

$$\mathbf{M} \equiv \begin{pmatrix} \mathbf{M_{qq}} & \mathbf{M_{qp}} \\ \mathbf{M_{pq}} & \mathbf{M_{pp}} \end{pmatrix} = \begin{pmatrix} \partial \mathbf{q}_t / \partial \mathbf{q}_0 & \partial \mathbf{q}_t / \partial \mathbf{p}_0 \\ \partial \mathbf{p}_t / \partial \mathbf{q}_0 & \partial \mathbf{p}_t / \partial \mathbf{p}_0 \end{pmatrix}. \tag{1.9}$$

The Maslov index comes from the fact that there are two possible branches when one performs square root on a complex number in the prefactor calculation. The correct one is the one ensuring continuity of the prefactor over time (that is the reason why one needs to monitor the prefactor along a trajectory)[14]. The resulting Maslov index is absorbed to the action in Eq. 1.6.

If one denote $\mathbf{z^T} \equiv \{\mathbf{q}, \mathbf{p}\}$ and $\mathbf{z_t^T} \equiv \{\mathbf{q_t}, \mathbf{p_t}\}$, the equations of propagating $\mathbf{z}_t$ and the monodromy matrix are given by,

$$\frac{d\mathbf{z}_t}{dt} = \mathbf{J} \cdot \frac{\partial H}{\partial \mathbf{z}_t}, \tag{1.10}$$

$$\frac{d\mathbf{M}}{dt} = \mathbf{J} \cdot \frac{\partial^2 H}{\partial \mathbf{z}_t \partial \mathbf{z}_t} \cdot \mathbf{M} \tag{1.11}$$

with the initial condition $\mathbf{q_0}$, $\mathbf{p_0}$, and $\mathbf{M}(t=0) = I$, the unitary matrix. The symplectic matrix $\mathbf{J}$ is defined as,

$$\mathbf{J} = \begin{pmatrix} 0 & I \\ -I & 0 \end{pmatrix} \tag{1.12}$$

The monodromy matrix has the following useful properties,

$$\mathbf{M^{-1}} \cdot \mathbf{J} = \mathbf{J} \cdot \mathbf{M^T} \tag{1.13}$$

For simplicity, in the remaining part of the thesis, if not specified, $\hbar$ is set to unity.

In many applications, calculations with the following matrix element are needed,

$$\langle \mathbf{p_f}, \mathbf{q_f}; \gamma_\mathbf{f} | e^{-i\hat{H}t} | \mathbf{p_i}, \mathbf{q_i}; \gamma_\mathbf{i} \rangle = (2\pi)^{-F} \int d\mathbf{p_0} \int d\mathbf{q_0}\, C_t(\mathbf{p_0}, \mathbf{q_0}) e^{i\Phi}, \tag{1.14}$$

where

$$\begin{aligned} \Phi &= S_t + \mathbf{p_0} \cdot (\mathbf{q_0} - \mathbf{q_i}) - \mathbf{p_t} \cdot (\mathbf{q_t} - \mathbf{q_f}) \\ &\quad + \frac{1}{2} \Delta \mathbf{z_0^T} \cdot \mathbf{\Gamma_i} \cdot \Delta \mathbf{z_0} + \frac{1}{2} \Delta \mathbf{z_t^T} \cdot \mathbf{\Gamma_f} \cdot \Delta \mathbf{z_t} \end{aligned} \tag{1.15}$$

where

$$\Delta \mathbf{z_0^T} = (\mathbf{q_0} - \mathbf{q_i}, \mathbf{p_0} - \mathbf{p_i}) \tag{1.16}$$

$$\Delta \mathbf{z_t^T} = (\mathbf{q_t} - \mathbf{q_f}, \mathbf{p_t} - \mathbf{p_f}) \tag{1.17}$$

$$\mathbf{\Gamma_i} = \begin{pmatrix} \frac{i\gamma\gamma_\mathbf{i}}{\gamma+\gamma_\mathbf{i}} & -\frac{\gamma}{\gamma+\gamma_\mathbf{i}} \\ -\frac{\gamma}{\gamma+\gamma_\mathbf{i}} & \frac{i}{\gamma+\gamma_\mathbf{i}} \end{pmatrix} \tag{1.18}$$

$$\mathbf{\Gamma_f} = \begin{pmatrix} \frac{i\gamma\gamma_\mathbf{f}}{\gamma+\gamma_\mathbf{f}} & \frac{\gamma}{\gamma+\gamma_\mathbf{f}} \\ \frac{\gamma}{\gamma+\gamma_\mathbf{f}} & \frac{i}{\gamma+\gamma_\mathbf{f}} \end{pmatrix} \tag{1.19}$$

The case $\gamma_f \to \infty$ corresponds to projecting the result to coordinate representation.

The derivatives of Φ are needed for various Filinov filtering methods,

$$\frac{\partial \Phi}{\partial \mathbf{z_0}} = \mathbf{\Gamma_i} \cdot \mathbf{J} \cdot \Delta \mathbf{z_0} - \mathbf{M^T} \cdot \mathbf{\Gamma_f} \cdot \mathbf{J} \cdot \Delta \mathbf{z_t}, \tag{1.20}$$

$$\frac{\partial^2 \Phi}{\partial \mathbf{z_0} \partial \mathbf{z_0}} = \mathbf{\Gamma_i} \cdot \mathbf{J} - \mathbf{M^T} \cdot \mathbf{\Gamma_f} \cdot \mathbf{J} \cdot \mathbf{M}, \tag{1.21}$$

$$\frac{\partial \Phi}{\partial \mathbf{z_t}} = -\mathbf{\Gamma_i} \cdot \mathbf{J} \cdot \Delta \mathbf{z_t} + \mathbf{M}^{-T} \cdot \mathbf{\Gamma_f} \cdot \mathbf{J} \cdot \Delta \mathbf{z_0}, \tag{1.22}$$

$$\frac{\partial^2 \Phi}{\partial \mathbf{z_t} \partial \mathbf{z_t}} = -\mathbf{\Gamma_i} \cdot \mathbf{J} + \mathbf{M^{-T}} \cdot \mathbf{\Gamma_f} \cdot \mathbf{J} \cdot \mathbf{M^{-1}}, \tag{1.23}$$

where one has used,

$$\left(\frac{\partial S}{\partial \mathbf{q_t}}\right)_{\mathbf{q_0}} = \mathbf{p_t} \tag{1.24}$$

$$\left(\frac{\partial S}{\partial \mathbf{q_0}}\right)_{\mathbf{q_t}} = -\mathbf{p_0} \tag{1.25}$$

In real applications, quite often one ends up with calculating the following quantity,

$$C_{AB}(t) = tr[\hat{A} e^{i\hat{H}t} \hat{B} e^{-i\hat{H}t}] \tag{1.26}$$

The SC-IVR result gives the following general result:

$$\begin{aligned} C_{AB}(t) &= \int d\mathbf{q_0} \int d\mathbf{q'_0} \int d\mathbf{p_0} \int d\mathbf{p'_0} \langle \mathbf{p_0}, \mathbf{q_0} \mid \hat{A} \mid \mathbf{p'_0}, \mathbf{q'_0} \rangle \langle \mathbf{p'_t}, \mathbf{q'_t} \mid \hat{B} \mid \mathbf{p_t}, \mathbf{q_t} \rangle \\ &\times \exp\{i[S_t(\mathbf{p_0}, \mathbf{q_0}) - S_t(\mathbf{p'_0}, \mathbf{q'_0})]\} \; C_t(p_0, q_0) \; C_t(p'_o, q'_0), \end{aligned} \tag{1.27}$$

where $\mathbf{q_t} = \mathbf{q_t}(\mathbf{p_0}, \mathbf{q_0})$ and $\mathbf{q_t} = \mathbf{q'_t}(\mathbf{p'_0}, \mathbf{q'_0})$. This is a double space calculation, which involves pairs of trajectories.

While each pair of trajectories in the above integrand are independent of each other, their contributions are damped by the coherent state product matrix, so only two trajectories close enough make significant contributions. This observation suggests further approximations of the SC-IVR formulation.

The forward-backward (FB) SC-IVR is based on the Fourier representation of the operator $\hat{B}$ (here for simplicity one assumes that $\hat{B}$ only depends on $\hat{\mathbf{q}}$)

$$B(\hat{\mathbf{q}}) = \int \frac{\mathbf{dp_s}}{(2\pi)^F} \tilde{B}(\mathbf{p_s}) e^{i\mathbf{p_s}\hat{\mathbf{q}}}. \tag{1.28}$$

Then one may focus on the unitary operator

$$\hat{U} = e^{i\hat{H}t} e^{i\mathbf{p_s}\hat{\mathbf{q}}} e^{-i\hat{H}t}, \tag{1.29}$$

which can be viewed as a single propagator with a time-dependent Hamiltonian[28–30a] (so only one trajectory is involved). In other words, the trajectory propagates in the following pattern,

$$\mathbf{p_0}, \mathbf{q_0} \rightarrow \ \mathbf{p_t}, \mathbf{q_t} \rightarrow \mathbf{p'_t} = \mathbf{p_t} + \mathbf{p_s}, \mathbf{q'_t} = \mathbf{q_t} \ \rightarrow \mathbf{p'_0}, \mathbf{q'_0}.$$

The FB-IVR formula for the correlation function is given by,

$$\begin{aligned} C_{AB}^{FB}(t) &= \int \frac{\mathbf{dp_s}}{(2\pi)^N} \tilde{B}(\mathbf{p_s}) \int \frac{\mathbf{dq_0 dp_0}}{(2\pi)^N} \\ & C_0(\mathbf{p_0}, \mathbf{q_0}; \mathbf{p_s})\, e^{iS_0(\mathbf{p_0},\mathbf{q_0};\mathbf{p_s})} \langle \mathbf{p_0 q_0} | \hat{A} | \mathbf{p'_0 q'_0} \rangle. \end{aligned} \tag{1.30}$$

The LSC-IVR formula is obtained by assuming that in the double space integration, only two trajectories very close make significant contributions. The basic formula is

$$C_{AB}(t) = tr[\hat{A} e^{i\hat{H}t} \hat{B} e^{-i\hat{H}t}] \approx \left(\frac{1}{2\pi}\right)^f \int d\mathbf{q_0} d\mathbf{p_0}\, A_w(\mathbf{q_0}, \mathbf{p_0}) B_w(\mathbf{q_t}, \mathbf{p_t}) \tag{1.31}$$

where A_w and B_w are the Wigner functions corresponding to these operators, *e.g.*,

$$A_w(\mathbf{q}, \mathbf{p}) = \int d\mathbf{\Delta q}\, e^{-i\mathbf{p}^T \cdot \mathbf{\Delta q}} \langle \mathbf{q} + \frac{\mathbf{\Delta q}}{2} | \hat{A} | \mathbf{q} - \frac{\mathbf{\Delta q}}{2} \rangle \tag{1.32}$$

1.3 Various Filtering Methods

To faciliate convergence of integrating an oscillatory function, the Filinov filtering method was developed[32]. The basic idea of the Filinov method is to do a coarse-graining of the integrand, so it becomes less oscillatory. The integral under interest is of the form

$$I = \int_{\infty}^{\infty} d\mathbf{z}\, f(\mathbf{z}) e^{i\Phi(\mathbf{z})}, \tag{1.33}$$

where $f(\mathbf{z})$ is a slowly varying function of $\mathbf{z}$, and $\Phi(\mathbf{z})$ is complex,

$$\Phi(\mathbf{z}) = \phi(\mathbf{z}) + i\theta(\mathbf{z}). \tag{1.34}$$

Then the following expression of unity

$$1 = \sqrt{\frac{|\alpha|}{\pi^F}} e^{(1/4)\beta^T\cdot\alpha^{-1}\cdot\beta} \int_{-\infty}^{\infty} d\mathbf{z_0}\, e^{-(\mathbf{z}-\mathbf{z_0})^T\cdot\alpha\cdot(\mathbf{z}-\mathbf{z_0})} e^{i\beta^T\cdot(\mathbf{z}-\mathbf{z_0})} \tag{1.35}$$

is inserted into the integrand of Eq. 1.33. Next $\Phi(\mathbf{z})$ is expanded quadratically around $\mathbf{z_0}$,

$$\Phi(\mathbf{z}) \approx \Phi(\mathbf{z_0}) + \Phi'(\mathbf{z_0})^T\cdot(\mathbf{z}-\mathbf{z_0}) + \frac{1}{2}(\mathbf{z}-\mathbf{z_0})\cdot\Phi''(\mathbf{z_0})\cdot(\mathbf{z}-\mathbf{z_0}) \tag{1.36}$$

where Φ' and Φ'' refer to,

$$\Phi'(\mathbf{z_0}) \equiv \frac{\partial\Phi(\mathbf{z_0})}{\partial\mathbf{z_0}} \tag{1.37}$$

$$\Phi''(\mathbf{z_0}) \equiv \frac{\partial^2\Phi(\mathbf{z_0})}{\partial\mathbf{z_0}\partial\mathbf{z_0}}. \tag{1.38}$$

The integration over $\mathbf{z}$ is done analytically, and one obtains,

$$\begin{aligned} I &= \int_{-\infty}^{\infty} d\mathbf{z_0}\, f(\mathbf{z_0}) \sqrt{\frac{2|\alpha|}{|2\alpha - i\Phi''|}} \\ &\exp\left[i\Phi + \frac{1}{4}\beta\cdot\alpha^{-1}\cdot\beta - \frac{1}{2}(\beta+\Phi')\cdot(2\alpha - i\Phi'')^{-1}\cdot(\beta+\Phi')\right]. \end{aligned} \tag{1.39}$$

In the above derivation, one assumes that $f(\mathbf{z})$ is a slowly varying function, therefore can be expanded over $\mathbf{z_0}$ and keep the constant term $f(\mathbf{z_0})$ only. In certain situation, it gives more accurate result if one include the dependence of $f(\mathbf{z})$ on $\mathbf{z}$. For example, in rate constant calculations, one confronts an integral in the form

$$I = \int_{\infty}^{\infty} d\mathbf{z}\, z_l e^{i\Phi(\mathbf{z})}, \tag{1.40}$$

After performing the above Filinov procedure, one ends up with

$$\begin{aligned} I &= \int_{-\infty}^{\infty} d\mathbf{z_0} \sqrt{\frac{2|\alpha|}{|2\alpha - i\Phi''|}} \left[z_l + i\sum_i (\beta+\Phi')_i (2\alpha - i\Phi'')^{-1}_{il}\right] \\ &\exp\left[i\Phi + \frac{1}{4}\beta\cdot\alpha^{-1}\cdot\beta - \frac{1}{2}(\beta+\Phi')\cdot(2\alpha - i\Phi'')^{-1}\cdot(\beta+\Phi')\right]. \end{aligned} \tag{1.41}$$

In a SC-IVR application of the Filinov method, there can be different decomposition of the integrand into $f(\mathbf{z})$ and $f(\Phi)$. The two ways usually adopted

in the literature are: a, $f(\mathbf{z})$ includes the prefactor, and all the terms appear in the exponent are assigned to Φ; b, only the imaginary part of the exponent is assigned to Φ, that is, Φ is real, and $f(\mathbf{z})$ includes all the remainings of the integrand. There are two set of parameters in Eq. 1.39 and Eq. 1.41: α and β. Various realizations of the Filinov filtering method in SC-IVR calculations can be obtained with different choices of these parameters and different decompositions of the integrand.

A method to reach (at least partially) stationary phase without resort to integration in complex plane is the Wang-Manolouplos-Miller version[33]. In this version, decomposition type a is adopted, and β is chosen as,

$$\beta = b\beta_0 = 2b\alpha \cdot \theta''(\mathbf{z_0})^{-1} \cdot \phi'(\mathbf{z_0}), \tag{1.42}$$

where b is a constant parameter within $[0, 1]$, and α is chosen as an diagonal constant matrix,

$$\alpha = a\mathbf{I}, \tag{1.43}$$

where $\mathbf{I}$ is the unity matrix. One may show that the gradient of the imaginary part of the exponent in Eq. 1.39 is approximately zero with the above choice of α and β_0. This method is probabily the best Filinov method one may construct for SC-IVR without resort to integration in complex plane. Numerical tests show dramatic improvement on the converging rate in some test systems. This method involves matrix inversion, which is in general computationally expensive for large systems (but see chaper 4). In addition, only if $\phi'' = 0$, the simple form of β_0 can be obtained from the stationary-phase condition. This may limit its application.

In all the versions of the Filinov filtering method discussed below, $\beta = 0$.

The basic idea of the Walton-Manolouplos version[17] is to choose α to be a diagonal matrix, and adopt decomposition a. This version also involves matrix inversion. Since the extra exponent term $[-1/2\Phi' \cdot (2\alpha - i\Phi'')^{-1} \cdot \Phi']$ in Eq. 1.39 can have positive real part, the diagonal elements of α should be sufficiently large to avoid blowing up of the integrand. Mathematically the blowing up is due to the fact that the expansion in Eq. 1.36 may result in an inverted gaussian.

This limitation of the values of α also applies to the Wang-Manolouplos-Miller version. Fortunately, in practice α is always chosen to be rather large so the filtering procedure does not distort the original integration significantly.

If α is given by $2\alpha - i\Phi'' = \mathbf{c}$, with $\mathbf{c}$ being a diagonal constant matrix, one reachs the Makri-Miller version[34]. Clearly, in this version no matrix inversion is needed.

In a series of Filinov filtering versions proposed by Herman[35], the main point is to adopt decomposition b, and to choose α as a constant diagonal matrix. This version is very simple to implement. Unlike other versions, this type of Filinov filtering is not exact for a gaussian integrand. However, in practice it usually gives quite good result since α is always chosen to be rather large. Another trick used by Herman is to expand the exponent over $\mathbf{z_t}$ rather than $\mathbf{z_0}$. The argument is that in Eq. 1.22 and 1.23 terms involving the final point $\mathbf{z_t}$ has no dependence on the monodromy matrix, and can be neglected. This may be advantageous if one calculates the wavefunction.

Chapter 2

Nonadiabatic Processes

2.1 Introduction

The correct description of electronically nonadiabatic processes is an active area of research in chemical reaction dynamics. Experimental and theoretical studies of excited electronic state dynamics have revealed that nonadiabatic interactions, such as intersections and avoided crossings of potential energy surfaces, are more the rule than the exception. This fact has profound implications for photochemistry, where the interesting dynamics begins on an electronic excited state. The purpose of this work is to test the performance of recent developments in semiclassical (SC) initial value representation (IVR) methods to describe the photodissociation dynamics of systems with multiple surface crossings.

In the context of a fully numerical solution of the Schrödinger equation, the modeling of dynamics on multiple coupled surfaces is straightforward[36]. A numerically exact integration of the Schrödinger equation, however, presents formidable computational challenges for all but the simplest few-body problems.[37]

Two classes of trajectory-based methods are popular in dynamics studies: surface-hopping models[38,39] and mean-field type (Ehrenfest) models[40]. While having found extensive applications, both methods have inherent problems that sometimes lead to serious errors.[41] A more rigorous, less *ad hoc* method is therefore desired.

McCurdy, Meyer, and Miller[42,43] introduced several ways of modelling the electronic degrees of freedom (DoF) involved in a nonadiabatic process by classical DoF, so that with a classical treatment also of the nuclear DoF one had a dynamically consistent description (at the classical level) of the complete vibronic dynamics. The particular version of these approaches proposed by Meyer and Miller (MM)[42] has proved most enduring, and a number of applications some twenty years ago showed it to work reasonablly well, though there are cases where it fails.[41,44] An important recent contribution was the interesting work of Stock and Thoss[22] which showed that if the MM hamiltonian were treated quantum mechanically, it would describe the original vibronic system exactly; *i.e.*, the MM hamiltonian is an exact quantum mapping of the original vibronic hamiltonian. Since the MM hamiltonian provides a classical model of the electronic DoF, however, one can also utilize it semiclassically with SC-IVR methods. This SC-IVR version of the MM model for electronically nonadiabatic processes has recently been tested for several 2 (electronic) - state systems: the 1 (nuclear)-dimensional model problems suggested by Tully for testing nonadiabatic dynamics,[45] for the spin-boson model for dissipative systems,[22,46] and for nonadiabatic dynamics of the ultrafast photodissociation of ozone[47], ICN[18i], and pyrazine[18j].

In this chapter we explore the capabilities of the SC-IVR approach to systems where more than two electronic surfaces are involved. To our knowledge this is the first test of SC-IVR methods for treating nonadiabatic dynamics of multichannel photodissociation reactions presenting more than one surface crossing. The test is performed for three model problems chosen in such a way to encompass different possibilities frequently found in photodissociation reactions. The differences between the models are the relative time scales on which the absorption and branching processes take place and the nature and proximity of the coupling between the PESs.

A linearized approximation to a full SC-IVR calculation was also tested in this work. Since the computational cost of this approximate method is only slightly more than that for an ordinary classical calculation, it is useful to explore its region of validity.

The chapter is organized as follows: Section 2.2 outlines the semiclassical approach for modeling nonadiabatic dynamics and defines the observables of interest, Section 2.3 presents the results for the three model problems defined below and compares them with full quantum calculations. Section 2.4 summarizes and concludes.

2.2 Theory

2.2.1 The Meyer-Miller Hamiltonian

The MM model introduces one classical DoF for each electronic state of the vibronic system. MM originally used action-angle variables for the "classical electronic DoF", though they employed the corresponding Cartesian variables for the actual trajectory calculations. Cartesian variables are the preferred choice for SC-IVR approaches, and in terms of them the MM Hamiltonian for a m-electronic state system is

$$H(\mathbf{P},\mathbf{R},\mathbf{p},\mathbf{x}) = \frac{\mathbf{P}^2}{2\mu} + \frac{1}{2}\sum_{i,j}[(p_i p_j + x_i x_j - \delta_{ij})ReV_{ij}(\mathbf{R}) + (p_i x_j - p_j x_i)ImV_{ij}(\mathbf{R})], \tag{2.1}$$

where $(\mathbf{P},\mathbf{R})$ and $(\mathbf{p},\mathbf{x})$ denote the nuclear and "electronic" variables, respectively, and $V_{ij}(\mathbf{R})$ is the diabatic electronic PES. (There is also an analogous expression for the adiabatic electronic representation.)

It should be emphasized that the "electronic" coordinates and momenta are not related to individual electrons, but rather describe the collective electronic manifold of m states. The m electronic states $\{|\ \phi_i\rangle\}$ correspond to the basis $\{|\ \phi_i\rangle = |\ 0_1 \cdots 0_{i-1} 1_i 0_{i+1} \cdots 0_m\rangle, i = 1, m\}$, where 0 and 1 refer to the ground state and the first-excited state, respectively, of a harmonic oscillator with unit mass and force constant. This basis is complete in the manifiold of states with one quantum of excitation in the m oscillators. (The total number of quanta in the m "electronic" oscillators is a constant of the motion, both classically and quantum mechanically.)

2.2.2 Evaluation of Observables by SC-IVR Methods

The total photo-absorption cross section $\sigma(\lambda)$, as a function of the photolysis wave length λ, is given by the Fourier transform of the survival amplitude $\xi(t)$,

$$\sigma(\lambda) = \frac{1}{2\pi}\int_{-\infty}^{\infty} dt\ \xi(t)\ e^{i\omega t} \equiv \frac{1}{2\pi}\int_{-\infty}^{\infty} dt\ \langle \Psi_i(\mathbf{R},\mathbf{x}) \mid e^{-i\hat{H}t/\hbar} \mid \Psi_i(\mathbf{R},\mathbf{x})\rangle\ e^{i\omega t} \tag{2.2}$$

where $\Psi_i(\mathbf{R},\mathbf{x}) = \psi_0(\mathbf{R})\phi_i(\mathbf{x})$, ψ_0 being the initial (typically the ground) vibrational state wavefunction for initial electronic state i.

The time dependent population of electronic state n is obtained as:

$$P_n(t) = \int d\mathbf{R} \mid \langle \phi_n, \mathbf{R} \mid e^{-i\hat{H}t} \mid \Psi_i\rangle \mid^2 \tag{2.3}$$

2.2.3 Linearized Approximation

The linearized approximation to the semiclassical method (LSC-IVR) leads to the classical Wigner model. In a LSC calculation, only coordinates and momentums are necessary to propagate, and no prefactor is involved, which greatly simplifies the calculation. Therefore, the LSC methods was also tested due to its simplicity and hence potential applications.

The transition probability from initial electronic state i to final electronic state f at time t corresponds to Eq. 1.31 with:

$$\hat{A} = \mid \Psi_i\rangle\langle\Psi_i \mid \tag{2.4}$$

$$\hat{B} = \mid \phi_f\rangle\langle\phi_f \mid \tag{2.5}$$

While the initial nuclear wavefunction ψ_0 is a gaussian wavepacket centered at (R_0, P_0), both A_w and B_w can be evaluated analytically,

$$A_w(\mathbf{R},\mathbf{P},\mathbf{x},\mathbf{p}) = \rho(\mathbf{R},\mathbf{P})\rho_i^{el}(\mathbf{x},\mathbf{p}) \tag{2.6}$$

$$B_w(\mathbf{R},\mathbf{P},\mathbf{x},\mathbf{p}) = \rho_f^{el}(\mathbf{x},\mathbf{p}) \tag{2.7}$$

V_{ij}	De_i	β_i	Re_i	A_{ij}	R_{ij}	a_{ij}	c_i
V_{11}	0.003	0.65	5.0				0.00
V_{22}	0.004	0.6	4.0				0.01
V_{33}	0.003	0.65	6.0				0.006
V_{12}				0.002	3.40	16.0	
V_{23}				0.002	4.80	16.0	

Table 2.1: Parameters (in a.u.) used in Model I

where,

$$\rho(\mathbf{R},\mathbf{P}) = 2e^{-\gamma(R-R_0)^2-(P-P_0)^2/\gamma)} \tag{2.8}$$

$$\rho_k^{el}(\mathbf{x},\mathbf{p}) = 2^{(N+1)}(x_k^2+p_k^2-\frac{1}{2})\exp[-\Sigma_{n=1}^{n=N}(x_n^2+p_n^2)] \tag{2.9}$$

2.3 Applications to Three-State Systems

2.3.1 Model Problems and Initial Conditions

Three model systems were studied, which physically correspond to the ultrafast dynamics on three coupled excited electronic states with one of them populated by a femtosecond laser pulse.

In all the models, the three diabatic potentials are assumed to be Morse type potentials:

$$V_i = De_i(1-e^{-\beta_i(x-Re_i)})^2 + c_i, \tag{2.10}$$

and the nonadiabatic coupling terms are taken to be of Gaussian form centered at the crossing points:

$$V_{ij} = A_{ij}e^{-a_{i,j}(x-R_{ij})^2}. \tag{2.11}$$

The potential curves are shown in Figure 2.1 and the numerical values of the parameters are given in Table 2.1, 2.2, and 2.3, respectively.

In the three models considered, the system is excited instantaneously from the harmonic ground state to excited state 1 at time zero. Therefore the initial

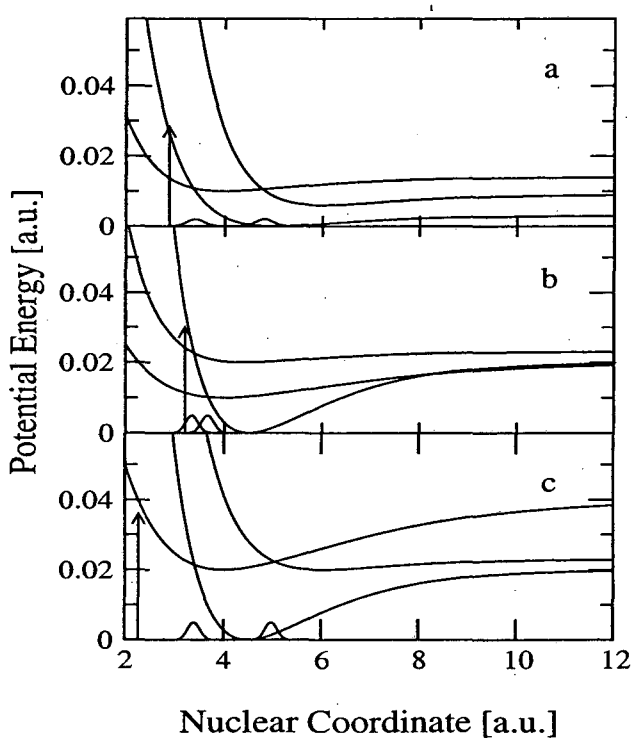

Figure 2.1: The diabatic PES for Model I, II and III (panels a,b and c repectively). The Gaussian non-adiabatic coupling is shown at the bottom. The position of the initial excitation is indicated by the arrow at the equilibrium geometry of the ground state. The parameters for each Model are given in Table 2.1.

V_{ij}	De_i	β_i	Re_i	A_{ij}	R_{ij}	a_{ij}	c_i
V_{11}	0.02	0.65	4.5				0.00
V_{22}	0.01	0.40	4.0				0.01
V_{33}	0.003	0.65	4.4				0.02
V_{12}				0.005	3.66	32.0	
V_{13}				0.005	3.34	32.0	

Table 2.2: Parameters (in a.u.) used in Model II

V_{ij}	De_i	β_i	Re_i	A_{ij}	R_{ij}	a_{ij}	c_i
V_{11}	0.02	0.4	4.0				0.02
V_{22}	0.02	0.65	4.5				0.00
V_{33}	0.003	0.65	6.0				0.02
V_{12}				0.005	3.4	32.0	
V_{13}				0.005	4.97	32.0	

Table 2.3: Parameters (in a.u) used in Model III

nuclear wavefunction is a Gaussian wave-packet centered at the ground state equilibrium bond length R_e and populated on state 1.

The three different models can be characterized as follows: In Model I the initial coupling V_{12} will first induce population transfer between states 1 and 2 and then the coupling is between states 2 and 3. The off-diagonal terms, V_{12} and V_{23}, are very well separated. In Model II, the branching processes occur at a shorter time and the initial coupling V_{12} is between states 1 and 2, and the second V_{13} between state 1 and state 3. Also, the off-diagonal coupling terms are very close to each other. Model III has non-vanishing coupling for V_{12} and V_{13}, except that the off-diagonal coupling terms are very well separated.

The nuclear mass m and ground state vibrational frequency ω are the same for the three models and equal to 20000 a.u. and $5\times\ 10^{-3}$ a.u. (1097 cm^{-1}), respectively. The value of R_e of the ground state from which the excitation is performed is denoted by the arrow in Figure 2.1. The values of R_e are 2.9, 3.3 and 2.1 a.u. for Models I, II, and III, respectively.

Full quantum mechanical results were obtained using the split-operator method[36].

2.3.2 Computational Details

The coherent state basis used for SC propagation was chosen to have the same width as the ground state wavefunction. To faciliate convergence, Herman's first order Filinov filtering method[35] was used in the full SC calculations for model I and II, with Filinov parameters $c = 40000$. No filtering was applied for model III, since numerical tests shows no improvement with filtering. For all the results reported in this work, a number of 300000 to 400000 trajectories were used to converge the results.

As can be seen from the MM hamiltonian, Eq. 2.1, the nuclear DoF may occasionally experience an inverted potential and move backward (to smaller R). While some of these trajectories may manage to move forward again, some of them may keep on gaining kinetic energy by moving along the inverted potential. In a fully converged calculation, contributions from these trajectories vanish; however, these trajectories usually have very large prefactors and introduce numerical instabilities. Including these trajectories (if the calculation can be numerically completed) may introduce severe contamination, and requires many more trajectories to converge the results. The usual way to deal with these unstable trajectories (as was done in all the full SC calculations reported in this work) is simply to drop them according to an *ad hoc* criterium[22]: for model I, II, and III, those trajectories with prefactor bigger than 10^8, 10^8, and 10^{10}, respectively. The number of dropped trajectories is only a small percentage (less than 1%)of the total number of trajectories, and has no significant effect on the final results.

In a recent paper[48] Coker *et. al.* have suggested dropping the δ_{ij} term in Eq. 2.1 (the zero-point energy of the "electronic" oscillain the classical equations of motion (though retaining it in the classical action). Though we find their arguments for this variation of approach to be rather dubious, it does eliminate the possibility of the coefficents of the diagonal terms $V_{ii}(\mathbf{R})$ becoming negative, so we tried this modified theory for our present examples. In all cases, however,

we found that it gave worse results than the standard version of the MM-SC-IVR procedure.

2.3.3 Absorption Spectrum and Survival Amplitudes

In Fig. 2.2 the real part and modulus of the semiclassical survival amplitudes $\xi(t)$ (dots) are compared to the corresponding quantum mechanical results (solid line) for the three models. With the exception of small deviations in the shape of the envelope of the survival amplitudes, one sees that the semiclassical results are in excellent agreement with the quantum mechanical calculations, both in terms of the frequencies and the relaxation times for the three model systems studied. The absorption spectra were calculated from the survival amplitudes by Eq. 2.2, and are shown in Fig. 2.4. One sees that the semiclassical photo-absorption spectra agree with quantum mechanical calculations well in terms of the shape and position of the absorption band. The small differences in the absorption intensities can be traced to small deviations in the survival amplitude envelope.

For model I, the ultrafast decay of the autocorrelation function happens within the first 18 fs after photo-excitation of the system. Absence of recurrences at longer times (panel a in Fig. 2.2) indicates that the photo-fragmentation process is direct, in the sense that the wave packet moves in the space of nuclear coordinates directly towards dissociation. Branching processes between the electronic states become important only after 15-20 fs (panel a, Fig. 2.5), when the system reaches the coupling region. Therefore, non-adiabatic couplings have only a minor effect on the absorption spectra and the spectrum shows no structure (panel a, Fig. 2.4).

The spectra corresponding to Model II (panel b in Fig. 2.4), at variance with Model I, presents a structure which is consistent with the presence of recurrences in the autocorrelation function(panel b in Fig. 2.2) . In this case branching processes becomes significant immediately after the excitation process. The presence of the coupling induces a back-and-forth electronic population transfer. This behavior is evidenced in the evolution of the electronic populations in panel b of

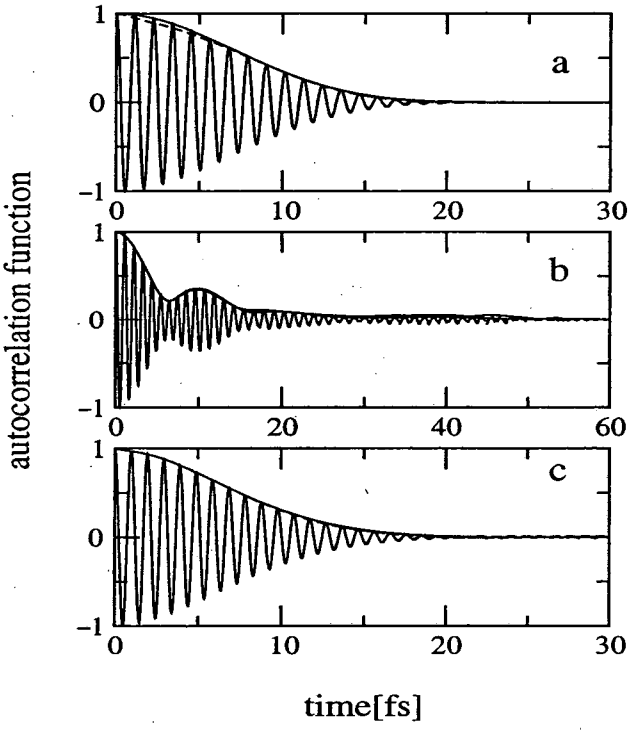

Figure 2.2: Comparison of the modulus and real part of the survival amplitudes associated with photo-excitation to electronic excited state 1 calculated according to the semiclassical methodology presented in section 2.2 (dashed line), compared with the corresponding quantum mechanical results (solid line). Panels (a), (b) and (c) show the results for Models I, II and III respectively.

Figure 2.3: Spectra

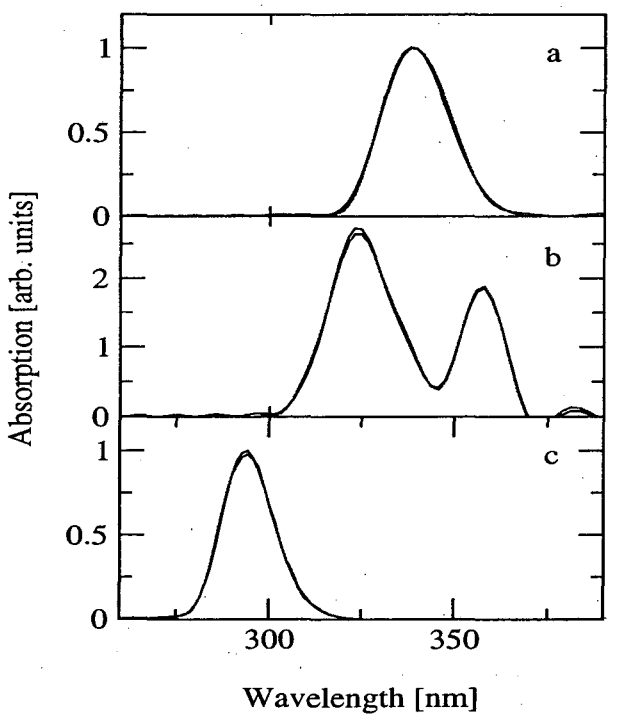

Figure 2.4: Comparison of the absorption spectra calculated according to the semiclassical methodology presented in section 2.2 (dotted line), compared with the corresponding quantum mechanical results (solid line). Panels (a), (b) and (c) show the results for Model I, II and III respectively. The slightly negative absorption coefficient in panel b is due to numerical errors.

Fig. 2.5(see discussion below).

For Model III, as in Model I, the dynamics of the photodissociation process is direct, and the non-adiabatic coupling has no effect in the determination of the absorption spectrum. Therefore the absorption spectrum is structureless(panel c, Fig. 2.4). The primary difference with model I is that in this case the autocorrelation function decays more slowly and consequently the absorption peak has a smaller width.

2.3.4 Evolution of the Electronic Populations

The evolution of the time-dependent electronic populations was calculated with the full SC-IVR methodology and also its linearized LSC-IVR version. Since the semiclassical propagator is not unitary, and there is "population leakage" associated with the Meyer-Miller Hamiltonian[22] , all the populations reported in this work have been renormalized so the sum of populations of the three states is always one.

The evolution of the time-dependent electronic populations for each model potential is shown in panels a, b and c in Fig. 2.5 for the Models I, II, and III, respectively. It is seen that at any time the evolution of the electronic state population calculated according to the SC-IVR presented above is in very good agreement with full quantum mechanical calculations. Each of the three models involves two branching processes. The difference between the models are the time at in which these process occurs and the states that are coupled. For Model I the branching process first occurs between the initially populated state 1 and state 2, and then there is a secondary population transfer between state 2 and state 3. For Models II and III the initially populated excited state 1 is coupled to two other electronic states; in Model II the branching processes occur in a much shorter time than for Model III. Model III thus presents the most expensive calculation since the branching processes occur on the longest time scale.

Finally, Fig. 2.6 shows the eletronic populations given by the linearized approximation to the SC-IVR, the LSC-IVR, compared to the accurate quantum

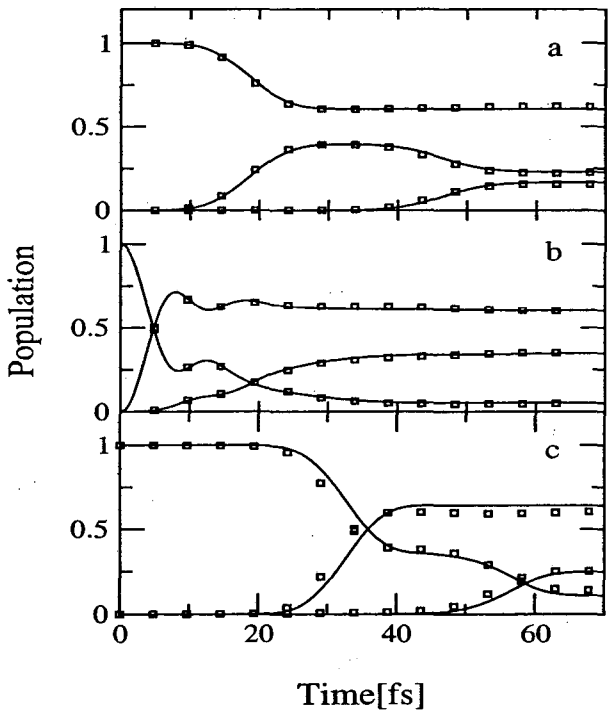

Figure 2.5: Evolution of the electronic populations $P_n(t)$ for each electronic state. SC-IVR (squares) are obtained according to the methodology presented in section 2.2. The solid line are the corresponding quantum mechanical results. Panel(a), (b) and (c) show the results for Model I, II and III respectively.

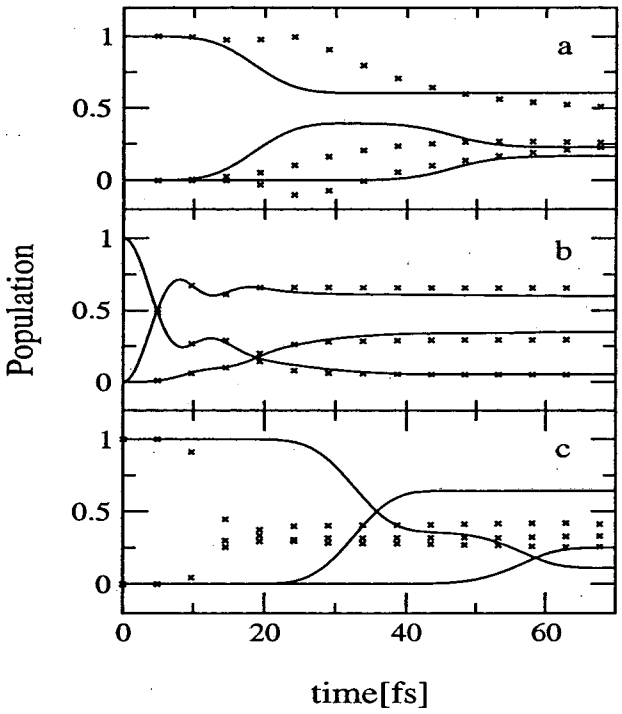

Figure 2.6: Evolution of the electronic populations $P_n(t)$ for each electronic state. LSC-IVR (crosses) are obtained according to the methodolgy presented in section 2.2. The solid line are the corresponding quantum mechanical results. Panel(a), (b) and (c) show the results for Model I, II and III respectively.

results. In an earlier work on thermal rate constants[30a], it is shown that quantum effects were well described by LSC-IVR for short time, but the longer time dynamics was purely classical. This is consistent with the results shown in Fig. 2.6. For Model II (panel b, Fig. 2.6) the simple LSC-IVR gives almost quantitative agreement for the evolution of the electronic populations because of the very fast time scale on which the branching processes is determined. For Models I and III, on the other hand, the LSC-IVR gives poor results (Fig. 2.6 panel a and c) , consistent with the fact that the branching processes have taken place in a longer time scale. One may notice that in Fig. 2.6a, one of the states has negative population at around 25 fs. This is due to the fact that populations calculated from the Wigner model are not always positive, as can be seen from Eq. 1.31 to Eq. 2.9.

2.4 Conclusions

In this work the capabilities of the Meyer-Miller hamiltonian with SC-IVR method have been tested to describe multichannel photodissociation reactions. For the three models considered, it is shown that the absorption spectra and the evolution of the populations in each electronic state, calculated by SC-IVR method, are in excellent agreement with full quantum mechanical calculations.

The LSC-IVR is much easier to apply than the full SC-IVR. As seen from the resulting expressions, it involves the overlap of the Wigner distribution function for the initial state with the classically time evolved Wigner distribution of the final state. The actual dynamics of the LSC-IVR is thus completely classical; the Wigner distribution provides the boundary conditions for the classical trajectories. As a consequence, the LSC-IVR approach provides a very good description for the model system where the non-adiabatic coupling occurs on a very short time scale, but it becomes less accurate as the nonadiabatic interaction occurs at longer times.

Chapter 3

Description of Tunneling

3.1 Introduction

It has been well-appreciated for a long time that the correct semiclassical description of tunneling (or, more generally, "classically forbidden") processes requires classical trajectories that explore complex-valued regions of phase space[49–54]. E.g., in the $1-d$ WKB approximation for barrier tunneling, the momentum of the particle is imaginary when it is inside the barrier. Recent work by Kay[55] and Heller *et. al.*[56,57] re-emphasizes this fact. For practical reasons, however— for example, if one wishes to use classical molecular dynamics to treat systems with many degrees of freedom—one would like to have at least an approximate way of describing tunneling-like phenomena that utilizes only real-valued classical trajectories, within either a fully classical or a semiclassical approach. Several examples of such approaches exist; e.g., a model used by Makri and Miller[58,59] (which is patterned after Tully's surface-hopping models for treating electronically non-adiabatic processes[60]) is a fairly primitive way of describing tunneling processes with only real-valued trajectories, but it has found some utility[61–67]. Within the semiclassical (SC) initial value representation (IVR) it has also been shown that purely real-valued classical trajectories can describe tunneling processes to a very useful extent[68–70]. (The very reason the IVR was first introduced[71], in fact, was to be able to describe classically forbidden vibrationally inelastic scattering with

real-valued trajectories.)

In this chapter we present another family of models for describing tunneling (or any classically forbidden) processes with real-valued classical trajectories; it can be implemented at a fully classical level, as described in Section 3.2, or much more accurately using the SC-IVR version of semiclassical theory, as described in Section 3.3. Some numerical tests are presented and discussed in Section 3.4.

3.2 The Model

We illustrate the model by application in this chapter to 1-dimensional barrier transmission, but one can easily imagine how models of this type could be applied more generally. The Hamiltonian of the system we consider is thus of the form

$$\hat{H} = \hat{P}^2/(2M) + V(\hat{R}), \tag{3.1}$$

where V(R) is a potential barrier in $1-d$, $-\infty < R < \infty$.

The model we propose was motivated by the McCurdy-Meyer-Miller model [43,72,73,42,74,18(f),22,20] for describing the electronic degrees of freedom (in electronically non-adiabatic processes) by auxiliary classical variables, but it can be stated more generally and independently of that work. Specifically, we introduce an auxiliary degree of freedom, a harmonic oscillator of unit frequency and mass, with coordinate and momentum operators $\hat{x}$ and $\hat{p}$; if the oscillator is in quantum state n, then since

$$\frac{1}{2}(\hat{p}^2 + \hat{x}^2)|\phi_n\rangle = (n + \frac{1}{2})|\phi_n\rangle \tag{3.2}$$

where we use units such that $\hbar = 1$, and $|\phi_n\rangle$ is the usual eigenstate of the harmonic oscillator, one has the identity,

$$\frac{1}{2}(\hat{p}^2 + \hat{x}^2 + 1 - 2n)|\phi_n\rangle = |\phi_n\rangle. \tag{3.3}$$

The Hamiltonian $\hat{H}(\hat{P}, \hat{R}, \hat{p}, \hat{x})$ in the expanded, $2-d$ space is now defined by

$$\hat{H}(\hat{P}, \hat{R}, \hat{p}, \hat{x}) = \hat{P}^2/(2M) + \alpha V(\hat{R}) + (1-\alpha)\frac{1}{2}(\hat{p}^2 + \hat{x}^2 + 1 - 2n)V(\hat{R}), \tag{3.4}$$

where α is an arbitrary parameter which in principle can take any value. We think of Eq. 3.4 as the Hamiltonian for a multichannel scattering problem, R being the scattering (or translational) coordinate and x the coordinate for the bound degree of freedom. It is clear that an exact wavefunction for Eq. 3.4 is

$$\Psi(R,x) = \phi_n(x)\psi(R), \tag{3.5}$$

and with this choice the quantum mechanics resulting from the Hamiltonian 3.4 is identical to that of the original $1-d$ Hamiltonian 3.1 (because

$$\frac{1}{2}(\hat{p}^2+\hat{x}^2+1-2n)V(\hat{R})|\phi_n\rangle|\psi\rangle = V(\hat{R})|\phi_n\rangle|\psi\rangle \quad). \tag{3.6}$$

Another way to look at Eq. 3.4 is to rewrite it in the following way:

$$\hat{H}(\hat{P},\hat{R},\hat{p},\hat{x}) = \hat{P}^2/(2M)+V(\hat{R})+[\frac{1}{2}(1-\alpha)(\hat{p}^2+\hat{x}^2+1-2n)+(\alpha-1)]V(\hat{R}); \tag{3.7}$$

the last term in the above expression is zero when operating on the wavefunction defined by Eq. 3.5, and therefore may be thought of as a pseudo "quantum" potential.

The classical (or semiclassical) model is now obtained by treating the 2d system classically; i.e., Hamiltonian 3.4 is taken to be a classical Hamiltonian. For definiteness (and also simplicity of application, below) we choose the state n of the auxiliary degree of freedom to be its ground state, $n = 0$, so that the classical Hamiltonian of the $2-d$ system becomes

$$H(P,R,p,x) = P^2/(2M) + \frac{1}{2}[(1-\alpha)(p^2+x^2)+1+\alpha]V(R). \tag{3.8}$$

To see the effect of the auxiliary degree of freedom at the classical level, we compute the transmission probability using the "classical Wigner" model, *i.e.*, a classical trajectory calculation with initial conditions chosen from the appropriate Wigner distribution function. The Wigner distribution for the ground state of the oscillator degree of freedom is

$$\rho_w(x_0,p_0) = e^{-2\epsilon_0}/\pi, \tag{3.9}$$

where $\epsilon_0 = \frac{1}{2}(p_0^2 + x_0^2)$, and the translational degree of freedom is taken to be a pure momentum state. Since $\frac{1}{2}(p^2 + x^2)$ is a constant of the motion (classically as well as quantum mechanically), a classical particle will be transmitted via the Hamiltonian 3.8 if, and only if, the initial translational energy E is greater than $[(1-\alpha)\epsilon_0 + \frac{1}{2}(1+\alpha)]V_b$, where V_b is the barrier height of V(R); *i.e.*, the auxiliary degree of freedom causes fluctuations in the barrier height. Averaging over the Wigner distribution of the auxiliary degree of freedom thus gives the transmission probability as

$$\mathcal{P}(E) = \int_0^\infty d\epsilon_0 \, 2e^{-2\epsilon_0} h\{E - [(1-\alpha)\epsilon_0 + \frac{1}{2}(1+\alpha)]V_b\}, \tag{3.10}$$

where $h\{\}$ is the Heaviside function,

$$h\{\xi\} = \begin{array}{ll} 1 & \text{if } \xi > 0, \\ 0 & \text{if } \xi < 0, \end{array}$$

and we have used the fact that

$$\int_{-\infty}^{\infty} dx_0 \int_{-\infty}^{\infty} dp_0 \, \{\quad\} = 2\pi \int_0^\infty d\epsilon_0 \{\quad\}; \tag{3.11}$$

evaluating the integral over ϵ_0 gives the final (classical) result

$$\mathcal{P}(E) = \{1 - \exp[\frac{-2(E - \frac{1}{2}(1+\alpha)V_b)}{(1-\alpha)V_b}]\}h[E - \frac{1}{2}(1+\alpha)V_b],$$

if $\alpha < 1$, and

$$h[E - \frac{1}{2}(1+\alpha)V_b] + \exp[\frac{-2(E - \frac{1}{2}(1+\alpha)V_b)}{(1-\alpha)V_b}]h[\frac{1}{2}(1+\alpha)V_b - E],$$

for $\alpha > 1$. (3.12)

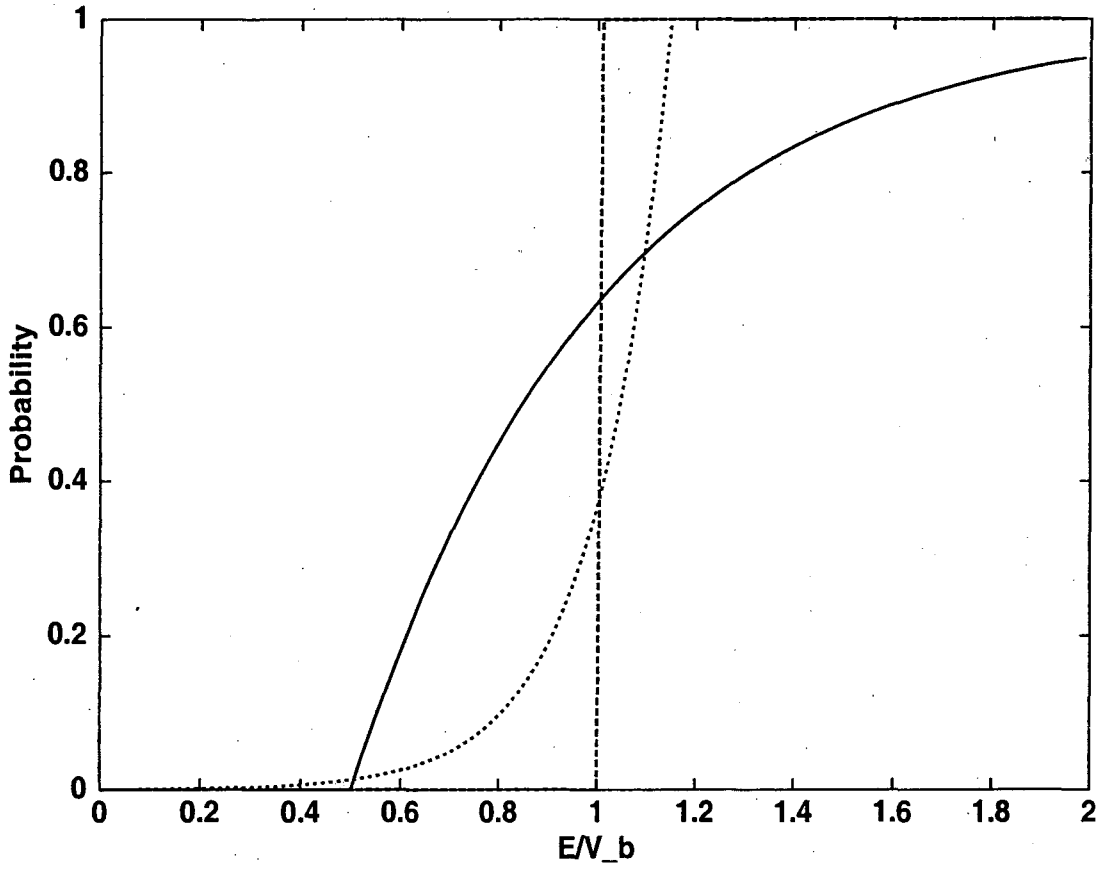

Figure 3.1: Transmission probability given by the classical treatment of the $2-d$ system, Eq. 3.12, for $\alpha = 0$ (solid line), $\alpha = 1$ (short-dashed line), and $\alpha = 1.3$ (long-dashed line).

If the parameter α is chosen to be 1, then (as is clear from Eq. 3.8) the auxiliary degree of freedom has no effect, and Eq. 3.10 reduces to

$$\mathcal{P}_{\alpha=1}(E) = h(E - V_b), \tag{3.13}$$

the classical transmission probability for the original $1-d$ barrier Hamiltonian 3.1. But for the choice $\alpha \neq 1$, one sees (cf. Figure 3.1) that Eq. 3.12 gives a result that qualitatively mimics the effects of tunneling. As noted above, this comes about because the classical distribution of energy in the auxiliary degree of freedom generates a distribution of barrier heights and thus some probability

of being transmitted at energies below the $1-d$ barrier height V_b (and reflected at energies above the barrier).

So we have the situation that if the $2-d$ system (with Hamiltonian 3.8) were treated fully quantum mechanically, the transmission probability would be the correct quantum value, indepdendent of the parameter α. Treated classically, the transmission probablility is not independent of α, and in fact for $\alpha \neq 1$ gives a finite transmission probablility for $E < V_b$ (and also a finite reflection probability for $E > V_b$).

In the next section we treat this $2-d$ system, Eq. 3.8, semiclassically, via the initial value representation.

3.3 The Semiclassical Initial Value Representation

The SC-IVR approach with HK propagator discussed in Chapter I was adopted here. For the present application the coordinates and momenta include both the translational degree of freedom, (R,P), and the auxiliary degree of freedom, (x,p), *i.e.*, $\mathbf{q}=(R,x)$ and $\mathbf{p}=(P,p)$.

The transmission probability can be expressed as the long time limit of a time correlation function,

$$\mathcal{P} = \lim_{t\to\infty} C_{AB}(t), \tag{3.14}$$

where

$$C_{AB}(t) = tr[\hat{A}e^{i\hat{H}t}\hat{B}e^{-i\hat{H}t}] \tag{3.15}$$

with operator $\hat{A}$ and $\hat{B}$ given by

$$\hat{A} = |\Psi_0\rangle\langle\Psi_0|, \tag{3.16}$$

$$\hat{B} = |\phi_0\rangle\langle\phi_0|h(\hat{R}). \tag{3.17}$$

The initial state $|\Psi_0\rangle$ is

$$|\Psi_0\rangle = |\phi_0\rangle|P_i,R_i,\gamma_i\rangle, \tag{3.18}$$

i.e., the ground state of the auxiliary degree of freedom and a coherent state for translation. For this particular case, the correlation function can also be expressed as

$$C_{AB}(t) = \int_0^\infty dR |\langle R|\langle \phi_0|e^{-i\hat{H}t}|\Psi_0\rangle|^2. \tag{3.19}$$

If the linearized SC approximation (LSC)[26,25] is applied to the IVR expression for the correlation function, then one obtains the classical Wigner approximation, Eq. 1.32.

3.4 Numerical Tests

The test system is chosen to be an Eckart potential[75],

$$V(R) = V_b \operatorname{sech}^2(R/a) \tag{3.20}$$

with parameters that correspond approximately to the $H + H_2$ reaction: $V_b = 0.425$ ev, $M = 1060$ a.u., and $a = 0.75$ a.u.. The initial center position for the translational coherent state is $R_i = -6.0$, with the coherent state parameter $\gamma_R = 0.5$; for the auxiliary degree of freedom $\gamma_x = 1$, and these same values for γ are also used for the coherent states in the SC propagator, Eq. 1.6. The translational coherent state is chosen rather broad in coordinate space so as to be fairly sharp in momentum space. Results are shown below as a function of the energy $E = P_i^2/(2M)$ corresponding to the center of the translational coherent state. The quantum results were calculated by the split-operator algorithm[76] for this same initial state.

Figure 3.2 shows the results of the SC-IVR calculation (the transmission probability is shown for $E < V_b$, and the reflection probablity for $E > V_b$), for several values of the parameter α, $\alpha = 0, 1, 1.3$, compared to the correct quantum values. $\alpha = 1$ corresponds to not having the auxiliary degree of freedom (cf. Eq. 3.4), and one sees that including it, i.e., $\alpha = 0$ or 1.3, gives better agreement with the quantum results. In particular, $\alpha = 0$ shows a very significant improvement and suggests itself as perhaps the 'universal' choice. $\alpha = 1.3$ gives very good results in the low energy tunneling region but less good results for over-barrier reflection.

For comparison, Figure 3.3 shows the results of the linearized SC approximation, *i.e.*, the classical Wigner model; this is the same as the classical result discussed in Section 3.1 except here averaged over the distribution of initial energy in the translational coherent state. One sees that there is much greater dependence on the α parameter than for the SC-IVR results in Figure 3.2, and thus less good agreement with the correct quantum values.

To focus more explicitly on the α-dependence of the SC-IVR results, Figure 3.4 shows the transmission probability as a function of α for one particular energy, $E = 0.4V_b$, fairly far into the tunneling region, for which the quantum transmission probability is 8×10^{-4}. To understand these results, as well as those in Figure 3.2, one may notice that the range the barrier can fluctuate is dependent on the value of α. For $\alpha < 1$, the whole potential varies from $(1 + \alpha)V/2$ to ∞. This sets a lower limit on the tunneling energy. For a given tunneling energy, α should be large enough so the barrier fluctuation range covers it. For $\alpha > 1$ the whole potential varies from $-\infty$ to $(1 + \alpha)V/2$. While there is no lower limit on the range the barrier can fluctuate, the weight of each barrier height is affected by the value of α. Therefore, in Figure 3.4, the tunneling probability increases when α is away from 1, since more trajectories can pass through the barrier. The semiclassical formulae discussed in this work are derived from the corresponding quantum formulae with the stationary-phase assumption. If the stationary-phase assumption is valid, one would expect the tunneling probability becomes independent of α once the value of α is sufficiently different from 1. For $\alpha > 1$, one does see the tunneling probability firstly increases quickly with α, then slows

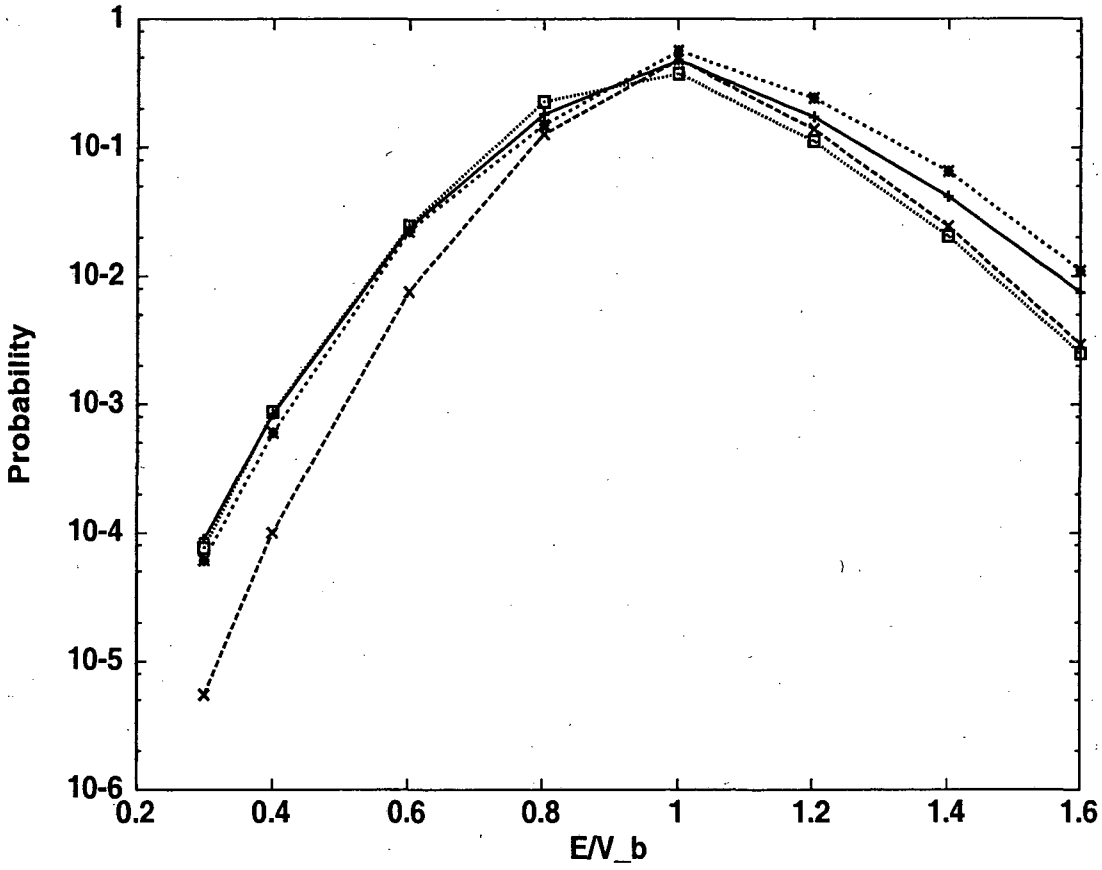

Figure 3.2: Transmission (for $E/V_b < 1$) and reflection (for $E/V_b \geq 1$) probabilities for the $1-d$ Eckhart barrier as a function of E/V_b. The values of α in Eq. 3.8 are: 0 (short-dashed line), 1 (long-dashed line), and 1.3 (dotted line). The solid line gives the correct quantum results. See the text for details.

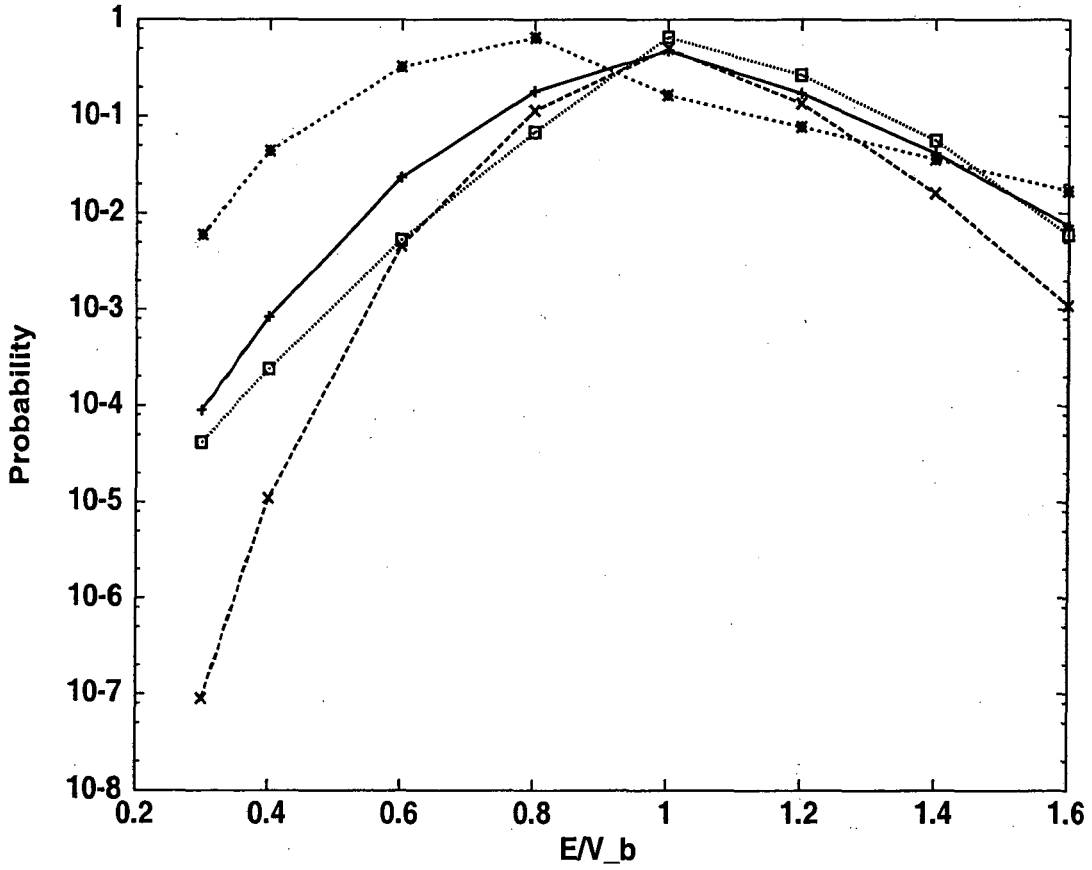

Figure 3.3: Transmission (for $E/V_b < 1$) and reflection (for $E/V_b \geq 1$) probabilities for the $1-d$ Eckart barrier as a function of E/V_b, given by the linearized SC (or classical Wigner) approximation , Eq. 1.32, for $\alpha = 0$ (short-dashed line), $\alpha = 1$ (long-dashed line), and $\alpha = 1.3$ (dotted line). For comparision, the correct quantum results are also shown (solid line).

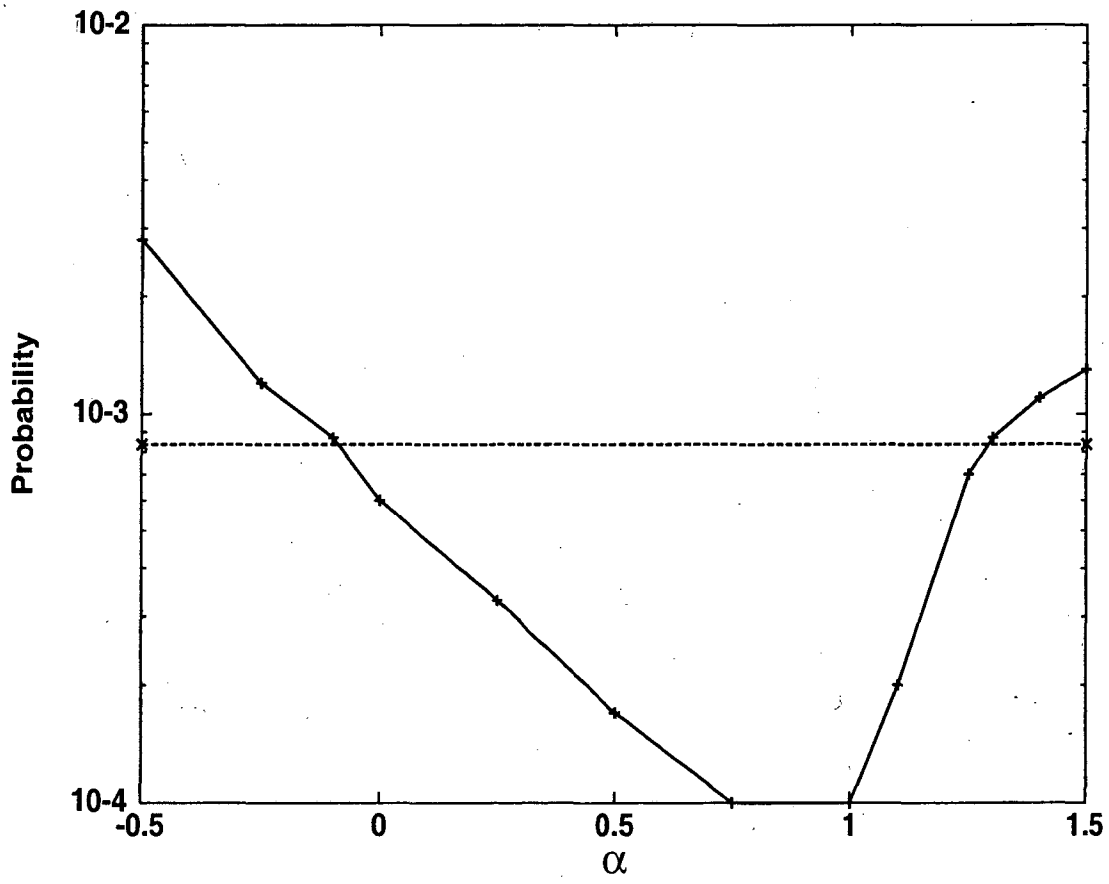

Figure 3.4: Transmission probabilities as a function of α in Eq. 3.8, for $E/V_b = 0.4$. Also shown is the correct quantum result (dashed line), which is independent of α.

down. For $\alpha < 1$, Hamiltonian 3.8 overemphasizes the tunneling trajectories—as can be seen from the classical results shown in Figure 3.1 and Figure 3.3. The final tunneling probability is due to mutual cancellation of contributions from these trajectories, which may result in large statistical errors. Therefore, choices of $\alpha > 1$ may have certain practical advantages.

Theoretically, the models discussed in this chapter can be understood in the following way:

For the bare hamiltonian 3.1, when the limit $\hbar \to 0$ is taken, only trajectories obeying classical mechanics survive. To give an accurate and unambiguous description of nonclassical tunnnelling and over-barrier reflection phenomena, one needs to resort to complex-valued trajectories. In the well-known "instanton" theory[11], for example, the tunneling path is generated by allowing the system to move along an inverted potential, which is accomplished by using imaginary time and momentum.

For the models discussed in this work, one expands the Hilbert space by adding some ficticious degrees of freedom. The role of this ficticious degree of freedom is to multiply the original bare potential by a varying factor. Therefore, the physical subsystem "feels" not only the original potential, but a whole ensemble of potentials with varying barrier height: some are higher than the physical potential, some are lower , and even inverted—"instanton"-like trajectories. In a quite different approach[77–79], Takatsuka and coworkers noticed that including only the instanton trajectories is not sufficient to describe tunneling in certain systems. Furthermore, the over-barrier reflection effect and the tunnelling effect are described on the same foot in the present approach, which can not be easily achieved by other semiclassical tunneling theories.

3.5 Concluding Remarks

In this chapter, we have discussed a class of semiclassical models for describing tunnelling with real-valued trajectories. While adding a fictitious degree of freedom is merely a mathematical trick, the underlying physics is to include clas-

sical trajectories that are "off the energy shell" of the original bare hamiltonian into the semiclassical calculation, an effect which has been shown to be essential for describing tunneling with real-valued classical trajectories.

There are several questions remaining open:

The form of the hamiltonian with one extra degree of freedom is clearly not unique. One may choose different values of α in Eq. 3.8. One may couple the fictitous degree freedom to the momentum term instead of the potential term of the bare hamiltonian 3.1. The question is how sensitive the tunneling probability depends on the hamiltonian form, and what is the best choice. The tunneling probabilities reported in this chapter are averaged over the energy distribution of the intial wavepacket. In the work of Grossman and Heller[56], the tunneling probabilities for definite energy states were calculated from a correlation function. Primitive results with this correlation type calculation show that the calculated semiclassical tunneling probabilities with the expanded hamiltonian Eq. 3.8 reproduce the analytic quantum results[80] down to a certain energy. Below this critical energy the results begin to deteriorate. The location of the critical energy varies with the value of α. This supports the idea that it is crucial that the range of fluctuations in the barrier of Hamiltonian 3.8 covers the tunneling energy under study. Further study along this line would be useful.

3.6 Appendix A

In this appendix we discuss numerical details on performing SC-IVR calculations.

First, let's make the following variable transformation:

$$x_0 = r_0 \cos(\theta_0) \tag{3.21}$$

$$p_0 = r_0 \sin(\theta_0) \tag{3.22}$$

Then, it can be shown that for the 1-state MM hamiltonian

$$H = \mathbf{P}^2/(2M) + V + \frac{1}{2}(x^2 + p^2 - 1)(1 - \alpha)V \tag{3.23}$$

r_0 is a constant of motion, and the electronic coordiate x and momentum p can be solved analytically:

$$x = p_0 \sin\zeta_t + x_0 \cos\zeta_t = r_0 \cos(\theta_0 - \zeta_t) \tag{3.24}$$

$$p = -x_0 \sin\zeta_t + p_0 \cos\zeta_t = p_0 \sin(\theta_0 - \zeta_t) \tag{3.25}$$

where ζ_t is defined to be:

$$\begin{aligned}\zeta_t &= (1-\alpha)\int_0^t dt\, V \\ &= \frac{2(1-\alpha)}{(1-\alpha)r_0^2 + (1+\alpha)}\left(Et - \frac{1}{2}\int_0^t dt\, \mathbf{P}\cdot\frac{d\mathbf{X}}{dt}\right) \qquad (3.26)\\ &= \frac{2(1-\alpha)}{(1-\alpha)r_0^2 + (1+\alpha)}\left(Et - \frac{1}{2}\int_{\mathbf{X_0}}^{\mathbf{X_t}} \mathbf{P}\cdot\mathbf{dX}\right) \qquad (3.27)\end{aligned}$$

with E to be the total energy. Therefore, ζ_t is related to the action with only the nucleus degree of freedom included. To be complete, one may also notice that the following term appeared in the action expression can also be integrated out analytically,

$$\begin{aligned}\int_0^t dt\, p\frac{dx}{dt} &= (1-\alpha)\int_0^t dt\, p^2 V \\ &= \frac{1}{2}r_0^2\zeta_t + \frac{1}{4}(p_0^2 - x_0^2)\sin(2\zeta_t) + x_0 p_0 \sin^2\zeta_t \qquad (3.28)\end{aligned}$$

Let's define vectors $\mathbf{z_t}$, $\mathbf{z_0}$, and the symplectic matrix J as

$$\mathbf{z_t} = \{\mathbf{X_t}, \mathbf{P_t}\} \tag{3.29}$$

$$\mathbf{z_0} = \{\mathbf{X_0}, \mathbf{P_0}\} \tag{3.30}$$

$$\mathbf{J} = \begin{pmatrix} 0 & I \\ -I & 0 \end{pmatrix} \tag{3.31}$$

In a semiclassical calculation, one may propagate all the necessary variables according to the following relations:

$$\frac{d\mathbf{z_t}}{dt} = \mathbf{J}\cdot\frac{\partial H}{\partial \mathbf{z_t}} \tag{3.32}$$

$$\frac{d}{dt}\left(\frac{\partial \mathbf{z_t}}{\partial \mathbf{z_0}}\right) = \mathbf{J}\cdot\frac{\partial^2 H}{\partial \mathbf{z_t}\partial \mathbf{z_t}}\cdot\frac{\partial \mathbf{z_t}}{\partial \mathbf{z_0}} \tag{3.33}$$

$$\frac{dS}{dt} = L \tag{3.34}$$

$$\frac{d\zeta_t}{dt} = \alpha V \tag{3.35}$$

$$\frac{d}{dt}\left(\frac{\partial \zeta_t}{\partial \mathbf{z_0}}\right) = \frac{\partial V}{\partial \mathbf{X_t}} \cdot \frac{\partial \mathbf{X_t}}{\partial \mathbf{z_0}} \tag{3.36}$$

$$\frac{d}{dt}\left(\frac{\partial \zeta_t}{\partial r_0}\right) = \frac{\partial V}{\partial \mathbf{X_t}} \cdot \frac{\partial \mathbf{X_t}}{\partial r_0} \tag{3.37}$$

$$\frac{d}{dt}\left(\frac{\partial \mathbf{z_t}}{\partial r_0}\right) = \frac{\partial}{\partial r_0}\left(\mathbf{J} \cdot \frac{\partial H}{\partial \mathbf{z_t}}\right) \tag{3.38}$$

The remaining monodromy matrix elements can easily be obtained from the above quantities through the chain rule, and will not be given here.

Similarly, for the MM hamiltonian $H = \frac{1}{2}(x^2 + p^2 - 1)(\mathbf{P}^2/(2M) + V(\mathbf{X})$, there are two constants of motion:

$$\epsilon_e = x^2 + p^2 - 1 = x_0^2 + p_0^2 - 1 \tag{3.39}$$

$$\epsilon_n = \mathbf{P}^2/(2M) + V(\mathbf{X}) = \mathbf{P}_0^2/(2M) + V(\mathbf{X_0}) \tag{3.40}$$

The electronic coordiate x and momentum p are again given in the form of 3.24 and 3.25, respectively, with the exception that α can be solved analytically in this case:

$$\alpha = \int_0^t dt\, \epsilon_n = \epsilon_n t \tag{3.41}$$

In a semiclassical calculation, the propagation variables and their time derivatives are as follows:

$$\mathbf{X}, \qquad \dot{\mathbf{X}} = \frac{\epsilon_e}{2}\mathbf{P}/M \tag{3.42}$$

$$\mathbf{P}, \qquad \dot{\mathbf{P}} = -\frac{\epsilon_e}{2}\frac{\partial V}{\partial \mathbf{X}} \tag{3.43}$$

$$\frac{\partial \mathbf{X}}{\partial \mathbf{X_0}}, \qquad \frac{\partial \dot{\mathbf{X}}}{\partial \mathbf{X_0}} = \frac{\epsilon_e}{2M}\frac{\partial \mathbf{P}}{\partial \mathbf{X_0}} \tag{3.44}$$

$$\frac{\partial \mathbf{X}}{\partial \mathbf{P_0}}, \qquad \frac{\partial \dot{\mathbf{X}}}{\partial \mathbf{P_0}} = \frac{\epsilon_e}{2M}\frac{\partial \mathbf{P}}{\partial \mathbf{P_0}} \tag{3.45}$$

$$\frac{\partial \mathbf{X}}{\partial \epsilon_e}, \qquad \frac{\partial \dot{\mathbf{X}}}{\partial \epsilon_e} = \frac{\epsilon_e}{2M}\frac{\partial \mathbf{P}}{\partial \epsilon_e} + \frac{\mathbf{P}}{2M} \tag{3.46}$$

$$\frac{\partial \mathbf{P}}{\partial \mathbf{X_0}}, \qquad \frac{\partial \dot{\mathbf{P}}}{\partial \mathbf{X_0}} = -\frac{\epsilon_e}{2}\frac{\partial^2 V}{\partial X \partial X} \cdot \frac{\partial \mathbf{X}}{\partial \mathbf{X_0}} \tag{3.47}$$

$$\frac{\partial \mathbf{P}}{\partial \mathbf{P_0}}, \qquad \frac{\partial \dot{\mathbf{P}}}{\partial \mathbf{P_0}} = -\frac{\epsilon_e}{2}\frac{\partial^2 V}{\partial X \partial X} \cdot \frac{\partial \mathbf{X}}{\partial \mathbf{P_0}} \tag{3.48}$$

$$\frac{\partial \mathbf{P}}{\partial \epsilon_e}, \qquad \frac{\partial \dot{\mathbf{P}}}{\partial \epsilon_e} = -\frac{\epsilon_e}{2}\frac{\partial^2 V}{\partial X \partial X} \cdot \frac{\partial \mathbf{X}}{\partial \epsilon_e} - \frac{1}{2}\frac{\partial V}{\partial \mathbf{X}} \tag{3.49}$$

The remaining elements of the monodromy matrix can be obtained easily from the above variables and the expressions of x and p.

Chapter 4

Thermal Rate Constants

4.1 Introduction

Calculation of thermal rate constants is one of the central tasks in theoretical studies of chemical dynamics. Given the potential energy surface (PES) of a system, one can define a dividing surface, which separates the PES into reactant and product region. A thermal rate constant measures how fast a system, initially in thermal equilibrium within the reactant region, moves to the product region. In principle, the thermal rate constant is independent of the choice of the dividing surface. Transition-state-theory (TST)[81,82] is widely used for thermal rate constant calculations. It describes the dynamics of a system by the thermodynamics of the system at the transition state region. Formulation of the theory is based on the no-recrossing assumption: trajectories cross over the dividing surface only once. Computer simulations with classical mechanics are also popular in the literature, and many numerical techniques have been developed for efficient calculations of large systems, e.g. the reaction path sampling method for sampling rare events[83]. For systems showing significant quantum effects including tunneling and interference, such as proton transfer reactions, a method beyond classical mechanics is required. The transition state theory was originally formulated as a classical theory. In the past several decades, many efforts have been made to develop a quantum version of the TST theory with some success[84,11,85–90]. Together

with the advance of computer technology, many algorithms for numerically exact quantum calculations have also been developed[76,36,92]. One method deserving mention is the multi-configuration time-dependent Hartree (MCTDH) method[1]. However, generally speaking, these exact methods are still restricted to relatively small systems. Therefore, further approximations are needed. Besides, for chemical systems, quantum effects are usually small or moderate, and full quantum calculations are unnecessary in many cases. This chapter will report some recent efforts to apply path-integral and various SC-IVR methods to the calculation of rate constants.

4.2 Theory

For simplicity, the mass-scaled coordinate is used throughout the chapter.

A formally exact expression for the thermal rate constant is given by the Miller-Schwartz-Tromp correlation functions[93,94],

$$k = \lim_{t\to\infty}\{\frac{C_{fs}}{Q_r}\} \tag{4.1}$$

$$= \frac{1}{Q_r}\int_0^\infty dt\, C_{ff}, \tag{4.2}$$

Where,

$$C_{fs} = tr[\hat{F}_\beta \hat{h}(t)], \tag{4.3}$$

$$C_{ff} = tr[\hat{F}_{\lambda\beta}\hat{F}_{(1-\lambda)\beta}(t)]. \tag{4.4}$$

In the above equations, an operator $\hat{A}(t)$ refers to a time-evolved operator,

$$\hat{A}(t) = \exp(i\hat{H}t)\hat{A}\exp(-i\hat{H}t). \tag{4.5}$$

The projection operator $\hat{h}$ is a function of the coordinates, and takes value 1 on the product region and 0 on the reactant region. The Boltzmannized flux operator $\hat{F}_\beta$ is defined as,

$$\hat{F}_\beta = \exp(-\beta\hat{H}/2)\hat{F}\exp(-\beta\hat{H}/2) = \exp(-\beta\hat{H}/2)\frac{1}{i}[\hat{H},\hat{h}]\exp(-\beta\hat{H}/2). \tag{4.6}$$

The constant λ can take any arbitrary value in $[0,1]$. $\hat{H}$ is the Hamiltonian operator of the system, and $\beta = (k_B T)^{-1}$. In the literature, C_{fs} and C_{ff} are called flux-side and flux-flux correlation functions, respectively. In this work, the imaginary and real time propagations were treated by path integrals and the semiclassical initial-value-representation method, respectively. The value of λ in the flux-flux correlation function form was taken as $1/2$.

In the following discussion, the hat on each operator is dropped, and $\hbar$ is set to 1.

4.2.1 The Path Integral Expression of the Boltzmannized Flux Operator

In coordinate representation, F is given by

$$\begin{aligned} F &= \int d\mathbf{x}\, |\mathbf{x}\rangle i[\frac{\mathbf{p}^2}{2}, h(s(\mathbf{x}))]\langle \mathbf{x}| \\ &= \int d\mathbf{x}\, |\mathbf{x}\rangle \frac{i}{2}\{\mathbf{p}[\mathbf{p}, h] + [\mathbf{p}, h]\mathbf{p}\}\langle \mathbf{x}| \\ &= \int d\mathbf{x}\, |\mathbf{x}\rangle \frac{1}{2}[\mathbf{p}\delta(s)\frac{\partial s}{\partial \mathbf{x}} + \delta(s)\frac{\partial s}{\partial \mathbf{x}}\mathbf{p}\langle \mathbf{x}|, \end{aligned} \tag{4.7}$$

where the function s defines the dividing surface. To derive a path-integral formulation of the Boltzmannized flux operator, let's review the usual procedure of deriving path-integral expression of the imaginary time propagator $\langle \mathbf{x}| \exp(-\beta H)|\mathbf{x}'\rangle$. One first splits the Boltzman operator into N pieces,

$$\langle \mathbf{x}| \exp(-\beta H)|\mathbf{x}'\rangle = \langle \mathbf{x}| \exp(-\Delta\beta H) \cdots \exp(-\Delta\beta H)|\mathbf{x}'\rangle, \tag{4.8}$$

where $\Delta\beta = \beta/N$. Then one applies the following Trotter splitting,

$$\exp(-\Delta\beta H) \approx \exp(-\Delta\beta T/2) \exp(-\Delta\beta V) \exp(-\Delta\beta T/2), \tag{4.9}$$

where $T = \mathbf{p}^2/2$ is the kinetic operator, and V is the potential operator. The final discrete path integral expression can be obtained by inserting the following identity

$$I = \int d\mathbf{x_i}\, |\mathbf{x_i}\rangle\langle \mathbf{x_i}| \tag{4.10}$$

in between terms of $\exp(-\Delta\beta T/2)$.

For semiclassical applications, one needs

$$\langle \mathbf{x_1}|\exp(-\Delta\beta T)|\mathbf{x_2}\rangle = \left(\frac{1}{2\pi\Delta\beta}\right)^{F/2}\exp[-\frac{1}{2\Delta\beta}(\mathbf{x_1}-\mathbf{x_2})^2], \tag{4.11}$$

and

$$\begin{aligned}
&\langle \mathbf{x_1}|\exp(-\Delta\beta T/2)F\exp(-\Delta\beta T/2)|\mathbf{x_2}\rangle \\
= &\frac{i}{2}\left(\frac{1}{\pi\Delta\beta}\right)^F\int d\mathbf{x}\delta(s(\mathbf{x}))\{\exp[-\frac{1}{\Delta\beta}(\mathbf{x}-\mathbf{x_1})^2]\frac{\partial s}{\partial \mathbf{x}}\cdot\frac{\partial}{\partial \mathbf{x}}\exp[-\frac{1}{\Delta\beta}(\mathbf{x}-\mathbf{x_2})^2] \\
&-\{\exp[-\frac{1}{\Delta\beta}(\mathbf{x}-\mathbf{x_2})^2]\frac{\partial s}{\partial \mathbf{x}}\cdot\frac{\partial}{\partial \mathbf{x}}\exp[-\frac{1}{\Delta\beta}(\mathbf{x}-\mathbf{x_1})^2]\} \\
= &\frac{i}{\Delta\beta}\left(\frac{1}{\pi\Delta\beta}\right)^F\int d\mathbf{x}\delta(s(\mathbf{x}))\frac{\partial s}{\partial \mathbf{x}}\cdot(\mathbf{x_2}-\mathbf{x_1}) \\
&\exp\{-\frac{1}{\Delta\beta}[(\mathbf{x}-\mathbf{x_1})^2+(\mathbf{x}-\mathbf{x_2})^2]\}
\end{aligned} \tag{4.12}$$

Putting everything together, a coherent-state matrix element of the flux-Boltzman operator is given by

$$\begin{aligned}
&\langle \mathbf{p_0 q_0},\gamma|\exp(-\beta H/2)F\exp(-\beta H/2)|\mathbf{p_0' q_0'},\gamma\rangle \\
= &\frac{i}{\Delta\beta}(\frac{4\gamma}{\pi})^{F/2}(\frac{1}{2\pi\Delta\beta})^{NF/2}\frac{1}{(1+\gamma\Delta\beta/2)^F} \\
&\int d\mathbf{x_1}\cdots d\mathbf{x_N}\int d\mathbf{x_s}\,\delta(s)\frac{\partial s}{\partial \mathbf{x_s}}\cdot(\mathbf{x_{N/2}}-\mathbf{x_{N/2+1}}) \\
&\exp\{-\frac{1}{2\Delta\beta}[\sum_{j=2}^{N/2}(\mathbf{x_j}-\mathbf{x_{j-1}})^2+\sum_{j=2+N/2}^{N}(\mathbf{x_j}-\mathbf{x_{j-1}})^2 \\
&+2(\mathbf{x_s}-\mathbf{x_{N/2}})^2+2(\mathbf{x_s}-\mathbf{x_{N/2+1}})^2] \\
&-\frac{1}{1+\gamma\Delta\beta/2}[\frac{\gamma}{2}(\mathbf{x_1}-\mathbf{q_0})^2+\frac{\gamma}{2}(\mathbf{x_N}-\mathbf{q_0'})^2+\frac{\Delta\beta}{4}(\mathbf{p_0}^2+\mathbf{p_0'}^2) \\
&+i\mathbf{p_0}\cdot(\mathbf{x_1}-\mathbf{q_0})-i\mathbf{p_0'}\cdot(\mathbf{x_N}-\mathbf{q_0'})]-\Delta\beta\sum_{j=1}^{N}V(\mathbf{x_j})\}.
\end{aligned} \tag{4.13}$$

The above expression can be viewed in the following way: the two phase points, $\{\mathbf{p_0},\mathbf{q_0}\}$ and $\{\mathbf{p_0'},\mathbf{q_0'}\}$, and a string of beads (which are weighted by $\Delta\beta V$) are connected by harmonic springs (with their strength determined by $\Delta\beta$); one effect of the flux operator is to force the middle one of the beads to lie on the dividing

surface. Compared with a coordinate-representation matrix element of the flux-Boltzman operator (which can be obtained by taking the limit $\gamma \to \infty$), Eq. 4.13 has extra imaginary terms, which introduce numerical difficulties on evaluating the matrix element. However, in the coherent-state representation, there exists a Gaussian damping factor for the momentum. This turns out to be of great advantage for semicalssical applications.

If one approximates $\delta s(\mathbf{x})$ by

$$\delta s(\mathbf{x}) \approx \delta(s(\bar{\mathbf{x}}) + \frac{\partial s}{\partial \bar{\mathbf{x}}} \cdot (\mathbf{x} - \bar{\mathbf{x}})) = \frac{1}{2\pi} \int_{-\infty}^{\infty} dp_s \, \exp\left\{ ip_s \left[s(\bar{\mathbf{x}}) + \frac{\partial s}{\partial \bar{\mathbf{x}}} \cdot (\mathbf{x} - \bar{\mathbf{x}}) \right] \right\}, \tag{4.14}$$

where $\bar{\mathbf{x}} = (\mathbf{x_1} + \mathbf{x_2})/2$, then

$$\begin{aligned} & \langle \mathbf{x_1} | \exp(-\Delta\beta T/2) F \exp(-\Delta\beta T/2) | \mathbf{x_2} \rangle \\ = \; & \langle \mathbf{x_1} | \exp(-\Delta\beta T) | \mathbf{x_2} \rangle \frac{1}{i\Delta\beta} \left(\frac{\partial s}{\partial \bar{\mathbf{x}}} \cdot \frac{\partial s}{\partial \bar{\mathbf{x}}} \right)^{-1/2} (\mathbf{x_2} - \mathbf{x_1}) \cdot \frac{\partial s}{\partial \bar{\mathbf{x}}} \\ & \exp\left[-\frac{2}{\Delta\beta} \left(\frac{\partial s}{\partial \bar{\mathbf{x}}} \cdot \frac{\partial s}{\partial \bar{\mathbf{x}}} \right)^{-1} s(\bar{\mathbf{x}})^2 \right]. \end{aligned} \tag{4.15}$$

This approximation removes the awkward δ function, and is supposed to be accurate if $\Delta\beta$ is sufficiently small (which means that the width of the Gaussian expression in Eq. 4.11 is small). The expression corresponding to Eq. 4.13 can be obtained easily, and will not be given here.

A special case is that a reaction coordinate q_1 can be identified, and the dividing surface is defined by q_1 only, e.g.

$$s = q_1. \tag{4.16}$$

Furthermore, the Hamiltonian of the system may be well approximated by a quadratic form, and the remaining non-quadratic terms are just small corrections. As an example, in a series of studies of a double-well linearly coupled to harmonic baths, Wang *et al*[25,26,30a] calculated the Boltzmannized flux operator matrix elements by approximating the Hamiltonian with a harmonic reference Hamiltonian, and the result agrees with the exact results well if the temperature is not too low.

In general, the potential of the system can be written as,

$$V = V(\mathbf{q_0}) - \frac{1}{2}\omega^{\dagger 2}(q_1 - q_{01})^2 + \frac{1}{2}\sum_{i=2}^{F}\omega_i^2(q_i - q_{0i})^2 + \Delta V, \tag{4.17}$$

and the Hamiltonian can be written as,

$$H = \sum_{i=1}^{F}\frac{1}{2}p_i^2 + V = H_0 + \Delta V, \tag{4.18}$$

where the reference Hamiltonian H_0 is defined as

$$H_0 = \frac{1}{2}p_1^2 - \frac{1}{2}\omega^{\dagger 2}(q_1 - q_{01})^2 + \sum_{i=2}^{F}[\frac{1}{2}p_i^2 + \frac{1}{2}\omega_i^2(q_i - q_{0i})^2] + V(q_0). \tag{4.19}$$

Instead of applying the Trotter splitting as in Eq. 4.9, one may adopt the following splitting,

$$\exp(-\Delta\beta H) \approx \exp(-\Delta\beta H_0/2)\exp(-\Delta\beta\Delta V)\exp(-\Delta\beta H_0/2). \tag{4.20}$$

With the following result,

$$\langle \mathbf{x_1}|\exp(-\Delta\beta H_0/2)|\mathbf{x_2}\rangle = \prod_{i=1}^{F}\sqrt{\frac{b_i}{2\pi}}\exp\left[-\frac{1}{2}a_i(x_{1i}^2 + x_{2i}^2) + b_i x_{1i}x_{2i}\right], \tag{4.21}$$

one has,

$$\begin{aligned}
&\langle \mathbf{p_0 q_0}, \gamma|\exp(-\beta H/2)F\exp(-\beta H/2)|\mathbf{p_0' q_0'}, \gamma\rangle \\
= &-\left(\frac{i}{2}\right)\frac{b_1^2}{d_1}\prod_{i=1}^{F}\left[\frac{b_i}{a_i+\gamma_i}\sqrt{\frac{\gamma_i}{\pi}}\left(\frac{d_i}{2\pi}\right)^{(N-1)/2}\right] \\
&\int d\mathbf{x_1}\cdots d\mathbf{x_N}\,[(x_{N/2})_1 - (x_{N/2+1})_1]\exp(\Phi),
\end{aligned} \tag{4.22}$$

where the exponent Φ is given by,

$$\begin{aligned}
\Phi = &-\sum_{i=1}^{F}\frac{1}{a_i+\gamma_i}[\frac{1}{2}(p_{0i}^2 + p'^2_{0i}) + \frac{1}{2}a_i\gamma_i(q_{0i}^2 + q'^2_{0i}) + \frac{a_i^2 + a_i\gamma_i - b_i^2}{2}(x_{1i}^2 + x_{Ni}^2) \\
&-b_i\gamma_i(x_{1i}q_{0i} + x_{Ni}q'_{0i}) + ip_{0i}(b_i x_{1i} - a_i q_{0i}) - ip'_{0i}(b_i x_{Ni} - a_i q'_{0i})] \\
&-\frac{1}{2}\sum_{j=2}^{N}[\mathbf{c(x_j^2 + x_{j-1}^2) - 2dx_j x_{j-1}}] - \Delta\beta\sum_{j=1}^{N}\Delta V(\mathbf{x_j}) \\
&-\frac{1}{2}[(a_1 - c_1)(x_{N/2,1}^2 + x_{N/2+1,1}^2) + 2d_1 x_{N/2,1}x_{N/2+1,1}].
\end{aligned} \tag{4.23}$$

In the above expressions,

$$a_i = \frac{\omega_i \cosh\left[\Delta\beta\omega_i/2\right]}{\sinh\left[\Delta\beta\omega_i/2\right]}, \tag{4.24}$$

$$b_i = \frac{\omega_i}{\sinh\left[\Delta\beta\omega_i/2\right]}, \tag{4.25}$$

$$c_i = \frac{\omega_i \cosh\left[\Delta\beta\omega_i\right]}{\sinh\left[\Delta\beta\omega_i\right]}, \tag{4.26}$$

$$d_i = \frac{\omega_i}{\sinh\left[\Delta\beta\omega_i\right]}. \tag{4.27}$$

For the reaction coordinate, $\omega_1 = i\omega^\ddagger$. Eq. 4.13 can be recovered by taking the limit $\omega \to 0$.

In the case that H can be well approximated by H_0, the coherent-state matrix element of the Boltzmannized flux operator is given analytically,

$$\langle \mathbf{p_0 q_0}, \gamma | \exp(-\beta H/2) F \exp(-\beta H/2) | \mathbf{p'_0 q'_0}, \gamma \rangle = \prod_{i=1}^{F} f_i, \tag{4.28}$$

where,

$$\begin{aligned} f_1 = & \left(\frac{\gamma_i}{\pi}\right)^{1/2} \left(\frac{B_i}{\gamma_i/2 + A_i}\right)^2 \frac{1}{2i} \left[(\gamma q'_{0i} + i p'_{0i}) - (\gamma q_{0i} - i p_{0i})\right] \\ & \exp\left[-\frac{\gamma_i}{2}\left(q_{0i}^2 + q'^2_{0i}\right) + i\left(p_{0i} q_{0i} - p'_{0i} q'_{0i}\right)\right] \\ & \exp\left[\frac{(\gamma q_{01} - i p_{01})^2 + (\gamma q'_{01} + i p'_{01})^2}{4(\gamma_i/2 + A_i)}\right], \end{aligned} \tag{4.29}$$

$$\begin{aligned} f_i = & \left(\frac{\gamma_1 B_1}{(\gamma_1/2 + A_1)^2 - B_1^2}\right)^{1/2} \exp\left[-\frac{\gamma_1}{2}\left(q_{01}^2 + q'^2_{01}\right) + i\left(p_{01} q_{01} - p'_{01} q'_{01}\right)\right] \\ & \exp\left[\frac{(\gamma_1/2 + A_1)\left[(\gamma q_{01} - i p_{01})^2 + (\gamma q'_{01} + i p'_{01})^2\right]}{4\left[(\gamma_1/2 + A_1)^2 - B_1^2\right]}\right] \\ & \exp\left[\frac{2B_1(\gamma q_{01} - i p_{01})(\gamma q'_{01} + i p'_{01})}{4\left[(\gamma_1/2 + A_1)^2 - B_1^2\right]}\right], \end{aligned} \tag{4.30}$$

with

$$A_1 = \frac{\omega^\ddagger \cos\left[\beta\omega^\ddagger/2\right]}{2\sin\left[\beta\omega^\ddagger/2\right]}, \tag{4.31}$$

$$B_1 = \frac{\omega^\ddagger}{2\sinh\left[\beta\omega^\ddagger/2\right]}, \tag{4.32}$$

$$A_{i\neq 1} = \frac{\omega_i \cosh[\beta\omega_i]}{2\sinh[\beta\omega_i]}, \tag{4.33}$$

$$B_{i\neq 1} = \frac{\omega_i}{2\sinh[\beta\omega_i]}. \tag{4.34}$$

This result was used by Wang *et. al*[30a] in their forward-backward SC-IVR studies of a double-well coupled to harmonic baths.

In the LSC approach, the Wigner function is needed, and is given by

$$\begin{aligned} F_W &= \frac{1}{(2\pi)^F}\int d\Delta\mathbf{q}\, e^{-i\mathbf{p}\cdot\Delta\mathbf{q}}\langle \mathbf{q}-\Delta\mathbf{q}|\exp(-\beta H/2)F\exp(-\beta H/2)|\mathbf{q}+\Delta\mathbf{q}\rangle \\ &= \frac{i}{\Delta\beta(2\pi)^F}\left(\frac{1}{\pi\Delta\beta}\right)^{(N+1)F/2}2^{(3-N)F/2} \\ &\quad \int d\mathbf{x_1}\cdots d\mathbf{x_N}\int d\mathbf{x_s}\,\delta(s)\frac{\partial s}{\partial \mathbf{x_s}}\cdot(\mathbf{x_{N/2}}-\mathbf{x_{N/2+1}}) \\ &\quad \exp\{-\frac{1}{2\Delta\beta}[\sum_{j=2}^{N/2}(\mathbf{x_j}-\mathbf{x_{j-1}})^2+\sum_{j=2+N/2}^{N}(\mathbf{x_j}-\mathbf{x_{j-1}})^2 \\ &\quad +(\mathbf{2q_0}-\mathbf{x_1}-\mathbf{x_N})^2+2(\mathbf{x_s}-\mathbf{x_{N/2}})^2+2(\mathbf{x_s}-\mathbf{x_{N/2+1}})^2] \\ &\quad -\Delta\beta\sum_{j=1}^{N}V(\mathbf{x_j})-\frac{\Delta\beta}{2}\mathbf{p}^2-i\mathbf{p}\cdot(\mathbf{x_1}-\mathbf{x_N})\} \end{aligned} \tag{4.35}$$

The expression corresponding to Eq. 4.22 is,

$$\begin{aligned} F_W &= -i\frac{b_1^2}{4\pi}\sqrt{\frac{2\pi}{d_1}}\prod_{i=1}^{F}\left[\sqrt{\frac{b_i^2}{\pi a_i}}\left(\frac{d_i}{2\pi}\right)^{(N-1)/2}\right]\int d\mathbf{x_1}\cdots d\mathbf{x_N}\,(x_{N/2,1}-x_{N/2+1,1}) \\ &\quad \exp\{-\sum_{\alpha=2}^{N}\sum_{i=1}^{F}[\frac{c_i}{2}(x_{\alpha i}^2+x_{\alpha-1,i}^2)-d_i x_{\alpha i}x_{\alpha-1,i}]-\frac{1}{2}\sum_{i=1}^{F}[a_i(2q_i^2+x_{1i}^2+x_{Ni}^2) \\ &\quad -2b_iq_i(x_{1i}+x_{Ni})-\frac{b_i^2}{2a_i}(x_{1i}-x_{Ni})^2+\frac{2}{a_i}p_i^2+2i\frac{b_i}{a_i}p_i(x_{1i}-x_{Ni})] \\ &\quad +\frac{1}{2}(c_1-a_1)(x_{N/2,1}^2+x_{N/2+1,1}^2)-d_1x_{N/2,1}x_{N/2+1,1} \\ &\quad -\Delta\beta\sum_{\alpha=1}^{N}V(\mathbf{x}_\alpha)\} \end{aligned} \tag{4.36}$$

The analytical expression of the Wigner function for a quadratic hamiltonian can be obtained[25], and is not given here.

4.2.2 The SC-IVR Approach

The standard Herman-Kluk semiclassical propagator was used to approximate the real-time propagator. The flux-flux correlation function involves two real-time propagators, and is evaluated by,

$$\begin{aligned} C_{ff}(t) &= \left(\frac{1}{2\pi}\right)^{2F} \int_{-\infty}^{\infty} \cdots \int_{-\infty}^{\infty} \mathbf{dp_0 dq_0 dp'_0 dq'_0}\, C_t(\mathbf{p_0}, \mathbf{q_0}) C'^{*}_t(\mathbf{p'_0}, \mathbf{q'_0}) \\ &\quad \exp\left[iS_t(\mathbf{p_0}, \mathbf{q_0}) - iS'_t(\mathbf{p'_0}, \mathbf{q'_0})\right] \langle \mathbf{p_0}, \mathbf{q_0}; \gamma | F_{\beta/2} | \mathbf{p'_0}, \mathbf{q'_0}; \gamma \rangle \\ &\quad \langle \mathbf{p'_t}, \mathbf{q'_t}; \gamma | F_{\beta/2} | \mathbf{p_t}, \mathbf{q_t}; \gamma \rangle. \end{aligned} \tag{4.37}$$

Therefore, trajectories need to be propagated in pairs. To obtain the thermal flux kQ_r, $C_{ff}(t)$ was evaluated at several time slices and integrated over t.

For FB/SC-IVR, with the Fourier representation of the Heaviside operator ,

$$h(\hat{q}_1) = \lim_{\epsilon \to 0^+} \int_{-\infty}^{\infty} dp_s \frac{1}{2\pi i (p_s - i\epsilon)} e^{ip_s \hat{q}_1}, \tag{4.38}$$

the fluxside correlation function is evaluated by,

$$C_{fs} = \left(\frac{1}{2\pi}\right)^{F} \int_0^{\infty} dp_s \frac{1}{\pi i p_s} C_{fb}(p_s) \tag{4.39}$$

$$\begin{aligned} C_{fb}(p_s) &= \int_{-\infty}^{\infty} \cdots \int_{-\infty}^{\infty} \mathbf{dp_0 dq_0}\, Im\{C_t(\mathbf{p_0}, \mathbf{q_0}) \\ &\quad \exp\left[iS_t(\mathbf{p_0}, \mathbf{q_0})\right] \langle \mathbf{p_0}, \mathbf{q_0}; \gamma | F_{\beta} | \mathbf{p'_0}, \mathbf{q'_0}; \gamma \rangle\}, \end{aligned} \tag{4.40}$$

where the trajectory propagates in the following way: $(\mathbf{p_0}, \mathbf{q_0}) \xrightarrow{t} (\mathbf{p_t}, \mathbf{q_t}) \rightarrow (\mathbf{p_t}, \mathbf{q_t}, p_{1t} + p_s) \xrightarrow{-t} (\mathbf{p'_0}, \mathbf{q'_0})$. The integration of p_s was done with a set of grid points of p_s, which means that several backward trajectories were calculated with each forward trajectory. In Eq. 4.39, the following property of the integrand $C_{fb}(p_s)$ is used: $C_{fb}(-p_s) = C_{fb}(p_s)^*$, which is easily seen by examining contributions from two identical trajectories with opposite propagation direction. Special considerations for the calculation of $C_{fb}(0)$ are discussed in the appendix.

The LSC-IVR results were calculated with

$$C_{fs} = \left(\frac{1}{2\pi}\right)^{F} \int_{-\infty}^{\infty} \cdots \int_{-\infty}^{\infty} \mathbf{dp_0 dq_0}\, F_W(\mathbf{p_0}, \mathbf{q_0}, \beta) h(q_1(t)) \tag{4.41}$$

4.2.3 Quantum Calculations Via a Discrete Variable Representation

The quantum rate constants were calculated via a discrete variable representation (DVR)[92]. Given an equally spaced grid for each degree of freedom q_α,

$$\begin{aligned} q_\alpha^{j_\alpha} &= j_\alpha \Delta q_\alpha, \\ j_\alpha &= 0, \pm 1, \pm 2, \cdots, \end{aligned} \tag{4.42}$$

where Δq_α is the grid spacing and $\alpha = 1, \cdots, F$. The Hamiltonian matrix $H_{j_1,\cdots,j_F;j'_1,\cdots,j'_F}$ is given by,

$$H_{j_1,\cdots,j_F;j'_1,\cdots,j'_F} = V(\mathbf{q_j}) \prod_{\alpha=1}^{F} \delta_{j_\alpha,j'_\alpha} + \sum_{\alpha=1}^{F} T^\alpha_{j_\alpha,j'_\alpha} \prod_{\beta=1,\beta\neq\alpha}^{F} \delta_{j_\beta j'_\beta}, \tag{4.43}$$

with

$$T^\alpha_{j_\alpha,j'_\alpha} = \frac{1}{2\Delta q_\alpha^2}(-1)^{j-j'} \left\{ \begin{array}{ll} \pi^2/3, & j = j' \\ 2/(j-j')^2, & j \neq j' \end{array} \right\}, \tag{4.44}$$

and δ_{ij} is the Kronick-delta function. After diagonalizing the Hamiltonian,

$$\mathbf{H} = \mathbf{U}^T \epsilon \mathbf{U}, \tag{4.45}$$

one has,

$$C_{ff}(t) = \sum_{k,k'} \exp\left[-\frac{1}{2}\beta(\epsilon_k + \epsilon_{k'})\right] \cos\left[(\epsilon_k - \epsilon_{k'})t\right] |\langle \epsilon_k | F | \epsilon_{k'} \rangle|^2 \tag{4.46}$$

with

$$\langle \epsilon_k | F | \epsilon_{k'} \rangle = \sum_{j_\alpha, j'_{\alpha'}} U^*_{j_\alpha,k} F_{j_\alpha,j'_{\alpha'}} U_{j'_{\alpha'},k'} \tag{4.47}$$

4.3 Numerical Tests

4.3.1 The Model

A model system involving a system coordinate s bilinearly coupled to a set of harmonic degrees of freedom $\{x_i\}$ was tested. Physically it describes a chemical reaction in condensed phase. This model was studied previously by McRae

et. al.[96], and Liao *et. al.*[97]. The system-bath Hamiltonian is given by,

$$H = \frac{1}{2}p_s^2 + V(s) + \frac{1}{2}\sum_i \left[p_{x_i}^2 + \left(\omega_i x_i - \frac{cs}{\omega_i}\right)^2\right]. \tag{4.48}$$

The potential $V(s)$ is chosen to be a symmetric Eckart potential with parameters mimicking the $H + H_2$ reaction in gas phase,

$$V(s) = V_0/\cosh^2(as/2\sqrt{m}), \tag{4.49}$$

where $a = 3.97\mathring{A}^{-1}$, $V_0 = 3428\ cm^{-1}$, and $m = 0.672\ amu$. The imaginary frequency at the top of the bare barrier is given by,

$$\omega^{\ddagger 2} = a^2 V_0/2m, \tag{4.50}$$

which is about 1100 cm^{-1}. The bath parameter is defined by a Gaussian friction kernel,

$$c_i^2 = \frac{2\eta\omega^{\ddagger 2}\sigma^2 \exp[-(\omega_i\sigma)^2/2]}{\tau(\omega_i\sigma)^2} \tag{4.51}$$

with $\omega_i = \pi/\tau(i-1/2)$, $i = 1, 2, \cdots, N$, $\tau = 2\sigma$ for $N = 1$, and $\tau = 5\sigma$ otherwise. Therefore, the bath is characterized by the friction strength η and the time scale σ. Three values of σ, 86.60, 18.48, and 3.696 fs, were considered in this work, corresponding to slow, medium, and fast solvent responses. Details of the model can be found in the paper of McRae *et. al.*[96].

For most of the calculations discussed below, normal mode coordinates were used, which are obtained by diagonalizing the force constant matrix at the transition state. One of the normal modes has imaginary frequency and is defined as the reaction coordinate.

4.3.2 Sampling Methods

In a SC-IVR calculation, a multi-dimensional complex function needs to be integrated. Choices of the sampling method and the sampling function turn out to be crucial for converging the integral.

a. Double Space SC-IVR

In the present work, the integration was done with a staging algorithm[91]: integrations over the auxiliary $\mathbf{x_i}$, the phase points $(\mathbf{p_0}, \mathbf{q_0})$, and $(\mathbf{p_0'}, \mathbf{q_0'})$, were done in stages. One reason for choosing the staging algorithm is to utilize the fact that the computational cost of integrating $\mathbf{x_i}$ is much less than that of integrating the phase points, which involves trajectory propagation. For convenience of the following discussion, each F-dimensional vector $\mathbf{x_i}$, $\mathbf{q_0}$, or $\mathbf{q_0'}$ will be called a bead. Two ways of implementing the staging algorithm were tested.

The first method utilizes the observation that the harmonic approximation, Eq. 4.28 - 4.34, is a good approximation in many situations. Therefore, the exponential part of the modulus of $\langle \mathbf{p_0}, \mathbf{q_0}; \gamma | F_{\beta/2} | \mathbf{p'_0}, \mathbf{q'_0}; \gamma \rangle$, given by Eq. 4.28, can serve as a sampling function for $(\mathbf{p_0}, \mathbf{q_0})$ and $(\mathbf{p'_0}, \mathbf{q'_0})$. Numerical tests show that using the diagonal elements of Eq. 4.28 as the sampling function gave faster convergence rate, and was adopted in the calculations reported below. The sampling function chosen in this way is a product of Gaussian and can be sampled by primitive Monte Carlo methods. In certain cases, the reaction coordinate frequency $\omega^\ddagger$ is so high that exponents of the gaussians are positive, then the value of $\omega^\ddagger$ was reduced to avoid this problem. Once the two trajectories were propagated, path integrals of the two Boltzmannized flux operators were calculated with primitive Monte Carlo. For each flux operator, the sampling function was chosen as the exponential part of the modulus of Eq. 4.22 with $\Delta V = 0$. The exponent of the sampling function is a Gaussian function, and defines a set of normal modes of the path integral beads $\{\mathbf{x_i}, \mathbf{i} = \mathbf{1}, \mathbf{N}\}$. Therefore, normal modes were first sampled with Gaussian distribution random number generator, then transformed back to $\{\mathbf{x_i}, i = 1, N\}$. In Eq. 4.37, the path integral $\langle \mathbf{p'_t}, \mathbf{q'_t}; \gamma | F_{\beta/2} | \mathbf{p_t}, \mathbf{q_t}; \gamma \rangle$ needs to be evaluated at each time slice. The same normal mode configuration can be used for all the time slices, since different boundary conditions at different time, which depend on $(\mathbf{p_t}, \mathbf{q_t}; \mathbf{p'_t}, \mathbf{q'_t})$, ensure different configurations in $\mathbf{x}$ space. To speed up convergence, for every pair of trajectories, path integral configurations were sampled $2000 \sim 5000$ times.

In the second method, the beads were divided into primary and secondary beads. The primary beads were sampled with Metropolis algorithm[98], and the

secondary beads were sampled by normal modes. Usually, the primary beads $\mathbf{X}$ include $\mathbf{q_0}$, $\mathbf{q'_0}$, and some of the path integral beads $\{\mathbf{x_i^I}\}$. The sampling function for the primary beads were chosen in this way: starting from the expression of $\langle \mathbf{p_0}, \mathbf{q_0}; \gamma | F_{\beta/2} | \mathbf{p'_0}, \mathbf{q'_0}; \gamma \rangle$, which is given by Eq. 4.13, approximate the potential terms of the secondary beads between two consecutive primary beads $\mathbf{x_i^I}$ and $\mathbf{x_j^I}$, to be a constant $(V(\mathbf{x_i^I}) + V(\mathbf{x_j^I}))/2$ (one may also include linear and quadratic terms of the Taylor series), and analytically integrate out those intermediate beads; the exponential part of the modulus of the resulting function was chosen as the sampling function for the primary beads. The secondary beads were sampled in a similar way as in method 1, and the normal modes of these bead were obtained with the above constant potential approximation, Therefore, the whole sampling procedure was as follows:

1. Make N_1 steps of Metropolis moves, then propagate the trajectories.

2. Perform N_2 (usually $N_2 >> N_1$) steps of normal mode sampling of the secondary beads. The normal model configurations were generated from a multi-dimensional Gaussian distribution. To speed up diffusion in the sampling space, for each step of normal mode sampling, step 1 was repeated with $\mathbf{q_0}$ and $\mathbf{q'_0}$ fixed (so no trajectory propagation is needed).

3. Repeat the above steps.

Sampling over $(\mathbf{p_0}, \mathbf{p'_0})$ was done with primitive Monte Carlo, since the sampling function of $(\mathbf{p_0}, \mathbf{p'_0})$ given by Eq. 4.13 is in Gaussian form. Every time $(\mathbf{q_0}, \mathbf{q'_0})$ moves, new values of $(\mathbf{p_0}, \mathbf{p'_0})$ were generated.

Instead of using two fixed numbers N_1 and N_2, one can also use a random number to control transitions between Metropolis moves and normal mode sampling. Numerical tests showed no noticeable difference between these two ways of controlling.

For the Metropolis method, one needs to calculate the normalization constant of the weighting function in order to obtain the reactive flux. With the current choice of the weighting function, it is equivalent to calculate the absolute value of $C_{ff}(0)$. For the current work, the absolute values of $C_{ff}(0)$ were obtained with the Gaussian sampling method discussed above. In general, one can always relate

the system under interest to another system with known results, similar to the case of free energy calculations in molecular simulations of liquids.

In a recent paper[95], Yamamoto *et. al.* suggested another version of the staging algorithm: sample the phase points $(\mathbf{p_0}, \mathbf{q_0})$ and $(\mathbf{p'_0}, \mathbf{q'_0})$ with the Metropolis algorithm, and the weighting function of which is obtained by converging the integrand of Eqn. 4.37 with fixed $(\mathbf{p_0}, \mathbf{q_0})$ and $(\mathbf{p'_0}, \mathbf{q'_0})$ at $t = 0$. In other words, the weighting function of the phase points is a renormalized function by integrating out the path integral degrees of freedom numerically. Compared with the two approaches discussed above, the advantage of this approach is that one has a better weighting function for the phase points, especially the momenta, and the number of trajectories needed to converge a SC-IVR calculation might be less. The disadvantage is that one needs to converge a multidimensional complex function at least once at every Metropolis step, which quickly becomes impractical when the system size increases. In addition, this procedure is not straightforwardly applicable to systems with a general dividing surface, since the extra terms about the middle path integral beads appearing in Eq. 4.13 and Eq. 4.35 can not be included in normal model samplings easily. One may combine the renormalization staging algorithm with the second method discussed above, and obtain the weighting function of the primary beads by integrating out the secondary beads numerically.

b. FB SC-IVR

Sampling methods of the FB SC-IVR calculations are similar to the double space calculations. Both the primitive and Metropolis MC methods are applicable to FB calculations. In this case, the exponential part of the diagonal element of the coherent matrix given by Eq. 4.28 in the primitive method, or by Eq. 4.13 in the Metropolis method is used for generating the sampling function.

The normalization constant calculation of the Metropolis method needs some special treatment, since $C_{fb}(0)$ is not easy to calculate directly. The method used in this work is based on the fact that the following quantity,

$$Z_s(\beta) = tr\left[\exp(-\beta\hat{H}/2)\delta(s)\exp(-\beta\hat{H}/2)\right], \tag{4.52}$$

which resembles the free energy of a constrained system, and its derivative,

$$\frac{\partial Z_s(\beta)}{\partial \beta} = tr\left[\exp(-\beta\hat{H}/2)(\hat{H}\delta(s) + \delta(s)\hat{H})\exp(-\beta\hat{H}/2)\right] \tag{4.53}$$

can be calculated with the same sampling function as in a FB calculation. Next, one tries to find out the absolute value of $Z_s(\beta)$ at one value of β, either deduced from a known rate constant, or by relating the system to a system (*e. g.*, a harmonic system), for which $Z_s(\beta)$ can be calculated directly. The second method is similar to the thermodynamic perturbation method one routinely uses to calculate free energies in a computer simulation[99]. Then, the normalization constant can be deduced from the absolute value and the relative value of $Z_s(\beta)$ obtained with a Metropolis sampling.

c. LSC-IVR

A LSC-IVR calculation uses Eq. 4.36 and the analytic Wigner function[25] of the quadratic hamiltonian to generate the sampling functions for the Metropolis and primitive samplings, respectively. Details including the normalization constant calculation are similar to the FB calculation.

The linearized approximation can also be applied to the flux-flux correlation function[95]. Implementation of the calculation is similar to the double space calculation, except that only a single space integration is needed, and the sampling functions are generated from the Wigner function.

4.3.3 Generalized Filinov Filtering

The coherent element of the Boltzmannized flux operator is complex, and a modified version of the Wang-Manolouplos-Miller Filinov filtering method[33] was designed to speed up convergence of its calculation. The integral under interest is of the form

$$I = \int_{\infty}^{\infty} d\mathbf{z}\, z_l e^{i\Phi(\mathbf{z})}, \tag{4.54}$$

Following a similar procedure as discussed in Chapter I, one reaches,

$$I = \int_{-\infty}^{\infty} d\mathbf{z_0} \sqrt{\frac{2|\alpha|}{|2\alpha - i\Phi''|}} \left[z_l + i\sum_i (\beta + \Phi')_i (2\alpha - i\Phi'')^{-1}_{il}\right]$$

$$\exp\left[i\Phi + \frac{1}{4}\beta\cdot\alpha^{-1}\cdot\beta - \frac{1}{2}(\beta+\Phi')\cdot(2\alpha - i\Phi'')^{-1}\cdot(\beta+\Phi')\right]. \quad (4.55)$$

Following Wang *et. al*, β is chosen as,

$$\beta = b\beta_0 = 2b\alpha\cdot\theta''(\mathbf{z_0})^{-1}\cdot\phi'(\mathbf{z_0}), \quad (4.56)$$

where b is a constant parameter between 0 and 1, and α is chosen as a diagonal constant matrix,

$$\alpha = a\mathbf{I}, \quad (4.57)$$

where $\mathbf{I}$ is the unity matrix.

A further approximation is to omit V'' while calculating θ''. This is justified since V'' should be much less than the contribution from the kinetic term (otherwise the number of beads should increase). With this approximation, the matrix inversions need only be done once at the beginning of the calculation, which greatly reduced the computational cost.

4.3.4 Numerical Details

In all the calculations, the total number of path integral beads for each degree of freedom ranged from 8 at 1000 K to 20 at 200 K. For fluxflux correlation function calculations, each of the flux operator calculations uses half of the beads.

The dividing surface is located at the transition state, perpendicular to the reaction coordinate q_1.

At quantum mechanics level, the calculated rate constant is independent of the coherent state widths, γ. However, in a SC-IVR calculation, the coherent state widths do affect convergence rate, and also affect accuracy of the final results slightly. For example, it has been numerically proved that results with a Herman-Kluk propagator (finite γ) is usually more stable and easier to converge than a Van-Vleck propagator ($\gamma \to \infty$). In a double-space SC-IVR calculation, values of γ should not be too big, otherwise only two trajectories very close at t make significant contribution to $C_{ff}(t)$, which dramatically increases sampling difficulties. On the other hand, one should avoid very small values of γ (to the

momentum representation limit) to fully utilize the advantage of the Herman-Kluk propagator with a Gaussian damping factor. In this work, values of γ were chosen as: $\gamma_1 = \omega^\ddagger \cot(\beta\omega^\ddagger/2)$, $\gamma_{i\neq 1} = \omega_i$.

In the Metropolis sampling method, a force-biased Metropolis algorithm[99] was used.

Eq. 4.28 was used to generate the weighting function of the phase points in the Gaussian sampling method. Eq. 4.22 was used for path integral calculations in both of the two sampling methods. The reference hamiltonian in Eq. 4.28 was based on the the normal mode frequencies at the transition state geometry. In the case that the temperature was too low, and the quadratic system has no meaningful rate constant defined, a reduced imaginary frequency would be used. The reference hamiltonian in Eq. 4.22 was not necessarily the same as that in Eq. 4.28. Instead, in some calculations frequencies of some modes were reduced so the reference hamiltonian in Eq. 4.22 does not deviate too much from the true potential when the coordinates were far away from the transition state point. Otherwise using the reference hamiltonian would reduce instead of increase the accuracy of path integral calculations (with the same number of beads).

For each pair of trajectories, the number of sampled path integral configurations was 2000 in the case of fast and medium solvent responses, and 5000 for slow responses. The exception is LSC calculations of the flux-side correlation functions, for which 20000 path-integral configurations were sampled for each Wigner function calculation (note that only one Wigner function element calculation was needed for each trajectory).

The filtering method discussed in Section 4.3.3 was used for all the semiclassical calculations. To choose the values of α and b, one first calculated several coherent state matrix elements with different choices of α and b, and selected the pair of values that filter most and still close enough to the converged unfiltered value of the matrix elements. Then the semiclassical calculations were performed with the selected filtering parameters. Fig. 4.1 shows a Wigner funcion element for a 10-medium response solvent mode model calculated with different values of b_0 and $\alpha = 60$. The temperature is 200K. Clearly convergence of the result was

$T(K)$	QM	SC	FB	$LSC1$	$LSC2$
1000	1.72e11	1.72e11	1.80e11	1.65e11	1.66e11
500	9.10e8	9.26e8	9.74e8	9.0e8	8.22e8
300	2.08e6	2.13e6	1.97e6	2.04e6	1.60e6
200	5.33e3	5.30e3	2.56e3		2.45e3

Table 4.1: Reactive flux for the 1-D Eckhart barrier.

η	QM	SC
0	9.54e1	9.29e1
2	5.92e-1	5.91e-1
5	1.63e-2	1.63e-2
8	1.35e-3	1.38e-3
10	3.32e-4	3.40e-4

Table 4.2: Reactive flux for the 2-D system-fast response bath at 200K.

greatly speeded up with filtering.

To save computer memory in quantum calculations, the following trick was adopted: grid points with energy larger than a cutoff energy E_c were discarded. The value of E_c was experimented with several calculations to ensure no noticeable effect on the calculated reactive flux values.

4.4 Results And Discussions

4.4.1 Double Space SC-IVR

The reactive flux of the 1-D Eckhart barrier was calculated at various temperatures, and the results were given in Table 4.1 and Fig. 4.2. All the calculations converged within 20000 pairs of trajectories. One may see that the double space SC-IVR results agree with exact quantum results very well.

Next, a set of 2-d systems with the barrier coupled to one harmonic bath were studied. The reactive fluxes were focused on 200K, at which the tunneling effect

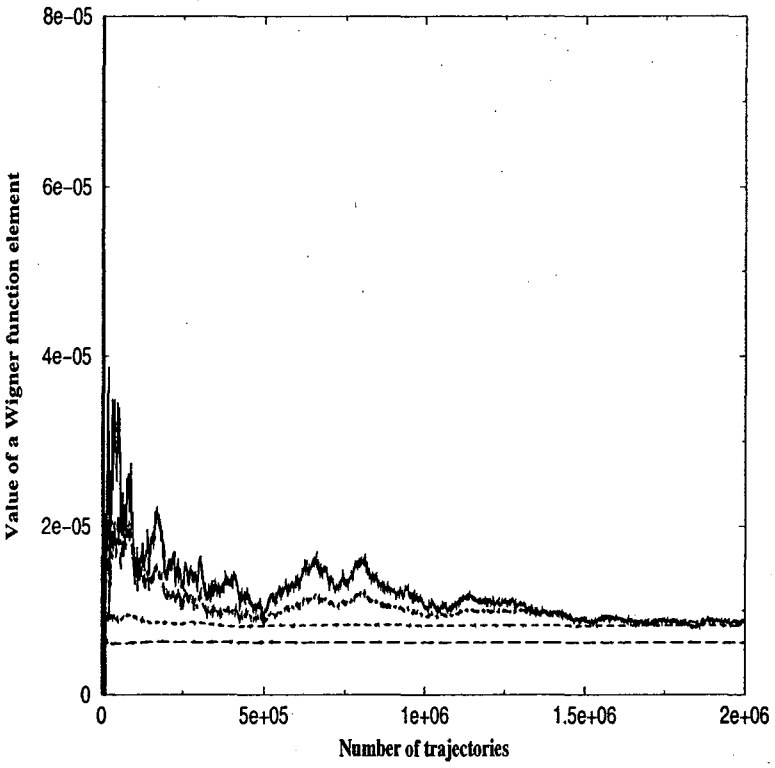

Figure 4.1: The value of a randomly selected Wigner function element calculated with various filtering parameters. The system has 10 medium response solvent modes, $T = 200K$, $\alpha = 60$, the value of β_0 takes 0.1 (dot-dashed), 0.5 (dashed), and 1 (long-dashed), respectively. The solid line is the unfiltered result, and the $\beta_0 = 0$ curve is indistinguishable from the unfiltered curve.

η	QM	SC	FB	$LSC1$	$LSC2$	$\omega^{\ddagger}$ (cm^{-1})
0	3.20e3	3.22e3			9.9e2	1164
1	5.93e2	6.14e2	1.1e3	1.0e3	3.4e2	927
3	6.87e1	6.96e1	9.45e1	6.50e1	4.1e1	654
5	1.40e1	1.42e1	1.50e1	1.39e1	1.18e1	522
10	1.30	1.30	1.29	1.21	1.26	374

Table 4.3: Reactive flux for the 2-D system-medium response bath at 200K.

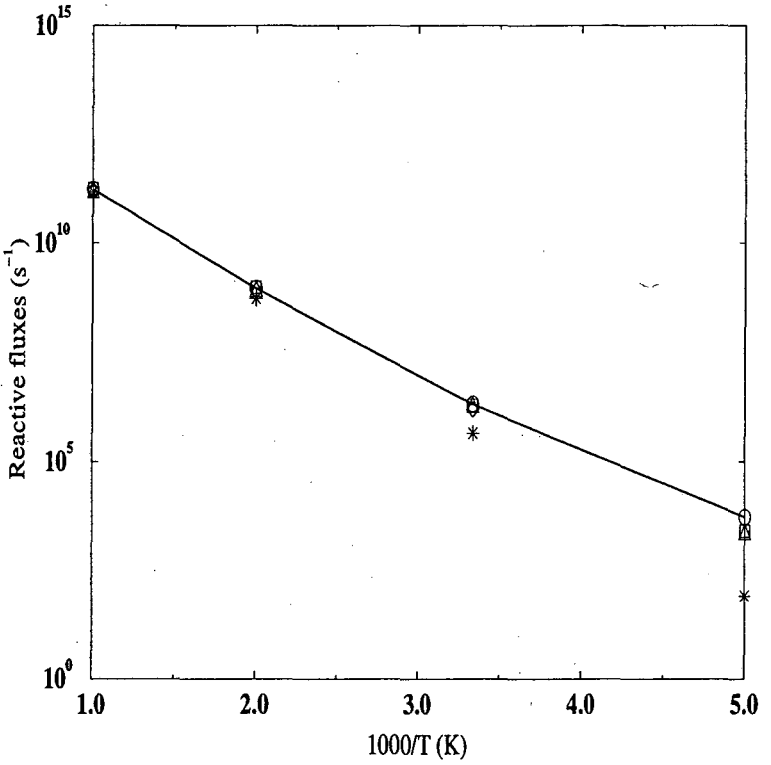

Figure 4.2: The reactive fluxes of the 1-D Eckhart barrier as a function of temperature calculated with various methods: QM (solid line), SC (cross), FB (squre), LSC1 (diamond), and LSC2 (triangle). The classical TST result is also shown for comparision (star).

η	QM	SC
0	1.40e4	1.47e4
3	4.78e3	4.65e3
5	2.59e3	2.47e3
8	8.27e2	1.01e3
10	5.57e2	7.59e2

Table 4.4: Reactive flux for the 2-D system-slow response bath at 200K.

is prominent. For fast and medium solvent responses, only 3000 to 10000 pairs of trajectories were needed to converge the double space SC-IVR calculations to within 5% statistical errors. The semiclassical and quantum results agree within 5%, and were show in Fig. 4.3. A flux-flux autocorrelation function for the model with medium solvent response and $\eta = 5$ is shown in Fig. 4.4, which reveals that the dynamics is straightforward, and recrossing is insignificant. This behavior is typical for the model with fast and medium solvent responses studied in Fig. 4.3. For this type of fast dynamics, a SC-IVR calculation is expected to converge easily.

For slow solvent responses, on the other hand, the dynamics becomes slower and recrossing shows manifest effect with increasing friction strength η. This behavior imposes difficulties on both quantum and semiclassical calculations. For quantum calculations, one need to use a very large grid to describe the system. For SC-IVR calculations, one need to run trajectories for longer time, which may result in larger prefactor, larger separation of two trajectories which may be close initially, and more oscillation of the integrand, all of which lead to harder convergence. For the calculations with $\eta \leq 5$ shown in Fig. 4.3, 10000 to 20000 pairs of trajectories were used, and the semiclassical results agree with the corresponding quantum results to within 5%. However, for the result of $\eta = 8$ shown in Fig. 4.3 and Fig. 4.4, 50000 pairs of trajectories were used. From Fig. 4.4 one sees that values of C_{ff} at time longer than 2000 a.u. are still not fully converged. The discrepancy between the SC-IVR flux and the quantum result is about 23%. It is even worse for $\eta = 10$. In Fig. 4.5, the upper figure shows the calculated C_{ff}. 50000 pairs of trajectories were used for the semiclassical calculations. While there is good agreement between the quantum and semiclassical results up to 3000 a.u., C_{ff} does not diminish afterwards, but keeps on oscillating around zero for much longer time. Both quantum and semiclassical calculations were extremely difficult in this case, and no converged results were obtained. This multi-recrossing behavior can be intuitively understood from the upper figures of Fig. 4.6 and Fig. 4.7. The normal model Hamiltonian, which is obtained from the force constant matrix of the full Hamiltonian at the transition

state configuration, deteriorates quickly while the system moves away from the transition state. Consequently, trajectories experience strong coupling between the two normal mode coordinates. For a typical trajectory, the reaction coordinate starts from the transition state region, then bounces back and forth by the potential, and it takes very long time for the system to fully leave the transition state. This back-and-forth behavior results in recrossing of the reaction flux. $C_{ff}(t)$ with recrossing takes much longer time to diminish, and the difficulty of converging a SC-IVR calculation increases with time. This recrossing behavior also explains why TST-type theories gave poor results[97], since the assumption of no-recrossing is violated. A possible solution is to rotate the coordinate (and so the dividing surface) to reduce recrossing. For simple systems like the 2-D model studied here, one may examine the potential energy surface directly to choose the new coordinate. In general, one may run a few trajectories with several choices of the coordinate, and pick up the one giving the fewest number of trajectories with back-and-forth behavior near the transition state region. In another study of $\eta = 10$, the normal mode coordinate was rotated 85 degrees anti-clockwise. The resulting potential energy surface under the new coordinate was shown in the lower figure of Fig. 4.6, and some typical trajectories were shown in the lower figure of Fig. 4.7. Clearly, these trajectories propagate directly away from the transition state region. The semiclassical C_{ff} was calculated with the Metropolis sampling method, and was shown in the lower figure of Fig. 4.5. Recrossing still exists, but is reduced. Values of C_{ff} at time shorter than 2000 a.u. were converged within 10000 pairs of trajectories, and agree well with quantum results. However, the part of C_{ff} at time longer than 2000 a.u. shows no significant improvement with additional trajectories. The final semicalssical result calculated with 50000 pairs of trajectories underestimates the flux by a factor of 2, with most of the error come from the long time part of C_{ff}.

The large errors of the SC-IVR results at long time set the limitation of current ways of implementing the method. Especially, the inability of making improvement with additional trajectories implies that the weighting function, which is based on only information at $t = 0$, is a bad choice if time is too

long, which is not surprising. A possible solution is to choose a time-dependent weighting function. To solve the normalization problem in practice, one may apply the umbrella sampling technique to the time domain: define a series of time windows, with overlaps between neighboring windows; choose one time-dependent sampling function for each window; connect these sections of C_{ff}, and calculate $C_{ff}(0)$ to obtain the flux.

For the current system, both of the two sampling methods discussed in Sec 4.3 work well. For systems described reasonably well by a reference harmonic Hamiltonian, the Gaussian sampling method is simpler. However, this method is limited by the requirements that the imaginary frequency can not be too high, and the dividing surface is a linear function of coordinates. While the first requirement can be relaxed by modifying the imaginary frequency of the reference Hamiltonian, as did above, the second requirement can not be relaxed easily. On the other hand, the Metropolis sampling method is generally applicable.

To test the numerical performance of the SC-IVR method, calculations were performed for a system with increasing number of medium response bath modes. The results are shown in Table 4.5. The SC-IVR calculation became more difficult to converge when the number of bath modes was increased. While calculation with a 5 bath mode system still could be converged within 30000 pairs of trajectories, for a 10 bath mode system, there was no clear hope of converging the result even after 10^5 pairs of trajectories.

In this work, the symmetrized flux-flux correlation function ($\lambda = 1/2$) was used. Therefore, path integral calculations were needed for every time slice. One may suggest to take ($\lambda = 1$), so only one path integral calculation at $t = 0$ is necessary. However, the symmetrized form has special numerical advantages. By rewriting

$$C_{ff}(t) = C_{ff}(0)\frac{C_{ff}(t)}{C_{ff}(0)}, \tag{4.58}$$

one sees that the order of magnitude of the flux is determined by the value of $C_{ff}(0)$, and accurate evaluation of $C_{ff}(0)$ is essential. For the symmetrized form, the two coherent state matrix elements in Eq. 4.37 at $t = 0$ are complex conjugate

n	QM	SC	FB	$LSC1$	$LSC2$
0	5.33e3	5.30e3	2.56e3		2.45e3
1	1.40e1	1.42e1	1.5e1	1.39e1	1.18e1
5		1.4e-2	1.5e-2	1.4e-2	1.0e-2
10			2.0e-14	2.2e-14	2.0e-14

Table 4.5: Reactive flux as a function of the number of medium-response bath modes at 200K

of each other, and the imaginary phases of these two elements cancel each other. At longer time, there is still partial cancellation of the phases, which results in a relatively smooth integrand, and greatly facilitate SC-IVR calculations. The price to pay is to repeat path integral calculations for each time slice.

4.4.2 FB SC-IVR

The FB calculations were focused on the medium solvent response case. From Table 4.1, 4.3, and 4.5, one can see that the FB and LSC results are similar in accuracy. Both give good results at high temperature. For systems with small system-bath coupling, which correspond to higher imaginary frequency $\omega^{\ddagger}$ and larger quantum effect (see Table 4.3), the FB and LSC results become less accurate. Generally speaking, the computational cost of a FB calculation is much higher than a LSC calculation. Especially, values of C_{fb} for small p_s are more difficult to converge, but these data points usually contribute most to the reactive flux (or rate constant). The one-bath mode calculation with $\eta = 0$ could not be converged even with 40000 forward trajectories. Fig. 4.8 shows the result of C_{fb} calculated as a function of p_s for a 5 solvent mode system. A number of 20000 forward trajectories were needed to converge the result. Therefore, the FB method may not be a good choice for rate constant calculations.

4.4.3 LSC-IVR

Results of the linearized approximation are denoted as LSC1 and LSC2 for the flux-side and flux-flux versions, respectively, and are given in Table 4.1, 4.3, and 4.5. Most of the LSC calculations were performed with 20000 to 40000 trajectories. Calculations show that the reactive fluxes calculated with the linearized flux-flux correlation function were less accurate than those calculated with the linearized flux-side correlation function. This conclusion is in agreement with what was found by Yamamoto *et. al.*. Fig. 4.9 clearly demonstrates that quantum coherence of the flux-flux correlation function can not be fully described by the linearized approximation. On the other hand, most of the quantum effects in a flux-side correlation function (especially at high temperature) is contained in the Boltzman operator, and is treated accurately by path integrals. However, a LSC1 calculation is usually more difficult to converge. The LSC1 calculations for the 1-D barrier, and the system-one medium response bath mode with $\eta = 0$ at 200K cannot converge even with 10^5 trajectories.

4.5 Conclusions

In this chapter, several ways of implementing the SC-IVR/PI methodology to reaction rate constant (or reactive flux) calculations were discussed. By testing on a model system, the calculated reaction fluxes agree well with quantum results, if the associated dynamics is not too slow. For slow, indirect dynamics, modifications on the current methods are needed, and some possible ways of improvement were discussed in the chapter. This work also reveals that PI/SC-IVR calculations become harder to converge at very low temperatures. One possible solution is to calculate low temperatures rate constants from the higher temperature results through analytic continuation, a method proved to be very accurate in previous studies[100]. In current study, the number of path integral beads was the same for all the degrees of freedom, which is an unnecessary constraint. One may use fewer beads for low frequency degrees of freedom to reduce the compu-

tational cost.

Formulations for the FB-IVR/PI and LSC/PI methodologies were also given and were tested with the model system. Calculations show that the FB-IVR/PI and LSC/PI methods give similar accuracy, but a LSC/PI calculation is computationally much less demanding. Both methods give good results if the temperature is not too low, or the barrier is not too narrow.

A way of implementing the modified generalized Filinov filtering method into coherent state PI calculations was also discussed. It was shown that the filtering method greatly accelerate the calculation.

4.6 Appendix

In the FB calculations of $C_{fb}(p_s)$, Eq. 4.40, $C_{fb}(0)$ can not be calculated directly. One way is to calculate C_{fb} for small p_s, and obtain $C_{fb}(0)$ by extrapolation. Another possibility is to calculate $C_{fb}(0)$ directly through L' Hopital's rule, which requires calculation of the following quantity,

$$\begin{aligned} C'_{fb}(p_s) &= -i\frac{\partial}{\partial p_s}\int_{-\infty}^{\infty}\cdots\int_{-\infty}^{\infty}\mathbf{dp_0 dq_0}\, C_t(\mathbf{p_0},\mathbf{q_0}) \\ &\quad \exp\left[iS_t(\mathbf{p_0},\mathbf{q_0})\right]\langle \mathbf{p_0},\mathbf{q_0};\gamma|F_\beta|\mathbf{p'_0},\mathbf{q'_0};\gamma\rangle|_{p_s=0}. \end{aligned} \tag{4.59}$$

One may easily recognize that this type of quantities has been studied by Thoss *et al*[31] on discussing the relation between LSC and differential FB, and the final expression is,

$$\begin{aligned} C'_{fb}(p_s) &= \int_{-\infty}^{\infty}\cdots\int_{-\infty}^{\infty}\mathbf{dp_0 dq_0}\, q_{1t}\left[1-\frac{1}{4}\sum_i(\gamma_i\frac{\partial^2}{\partial q_{0i}^2}-\frac{1}{\gamma_i}\frac{\partial^2}{\partial p_{0i}^2})\right] \\ &\quad \langle \mathbf{p_0},\mathbf{q_0};\gamma|F_\beta|\mathbf{p_0},\mathbf{q_0};\gamma\rangle. \end{aligned} \tag{4.60}$$

Numerical test shows that for a free particle system $C_{fb}(0)$ calculated by these two methods agree with each other. However in general applications, Eq. 4.60 is hard to converge due to the fact that integration over a scattered distribution of q_{1t} is needed. In all the FB calculations reported in this chapter, the extrapolation method was used.

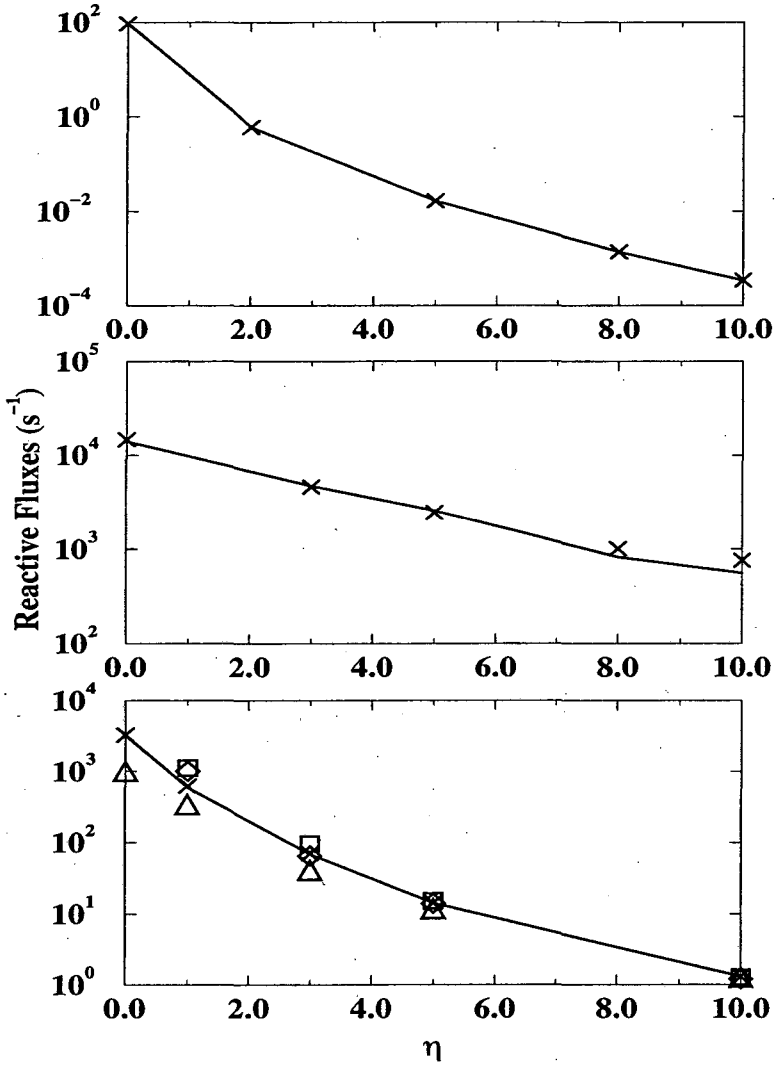

Figure 4.3: The reactive fluxes as a function of the friction parameter η. From upper to bottom, fast, slow, and medium solvent responses, respectively. Symbols are the same as in Fig. 4.2.

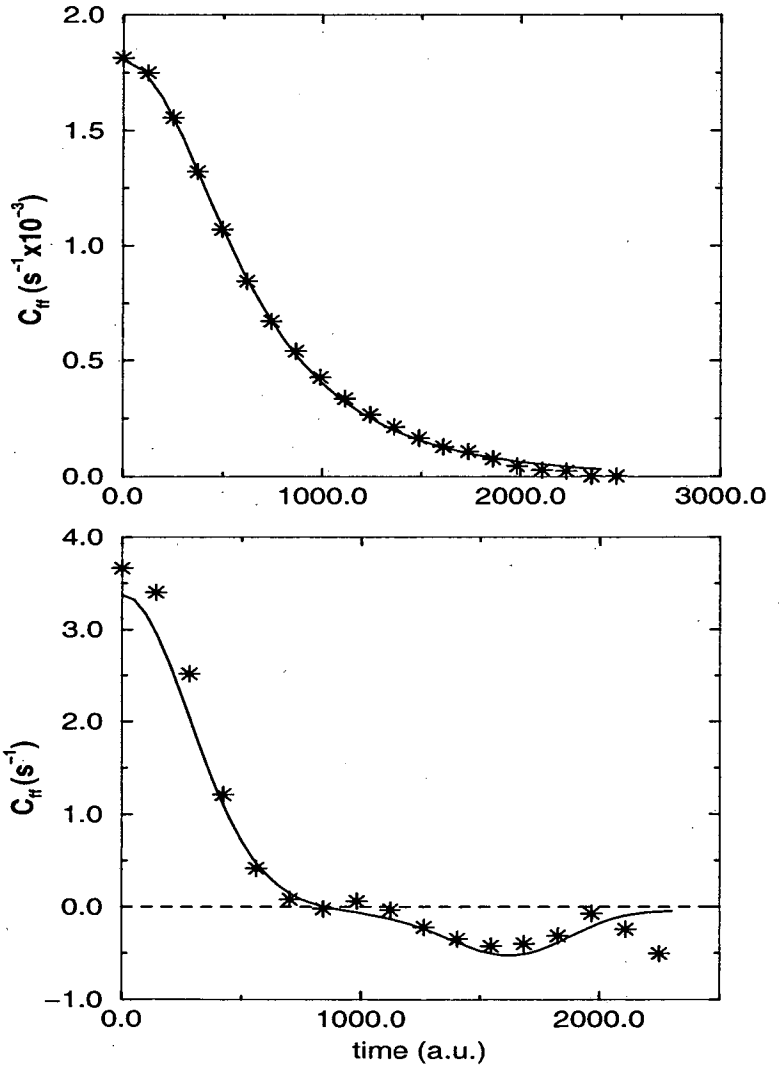

Figure 4.4: C_{ff} as a function of time (in atomic unit) calculated with quantum DVR method (solid line) and SC-IVR (stars). Upper: medium response, $\eta = 10$; bottom: slow response, $\eta = 8$.

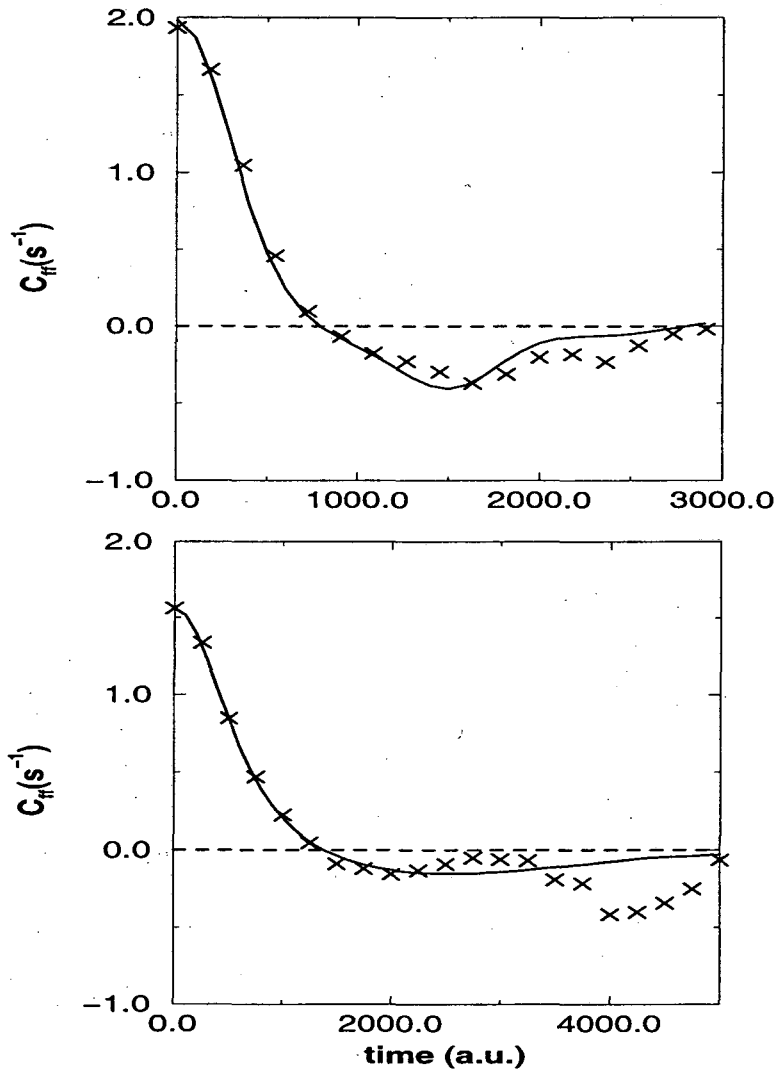

Figure 4.5: C_{ff} as a function of time (in atomic unit) calculated with quantum DVR method (solid line) and SC-IVR (stars). Both two figures are for slow solvent responses with $\eta = 10$. The difference is that the dividing surface of the upper one was based on the normal mode coordinate, and that of the lower one was chosen by rotating the normal mode coordinate. See Fig. 4.6.

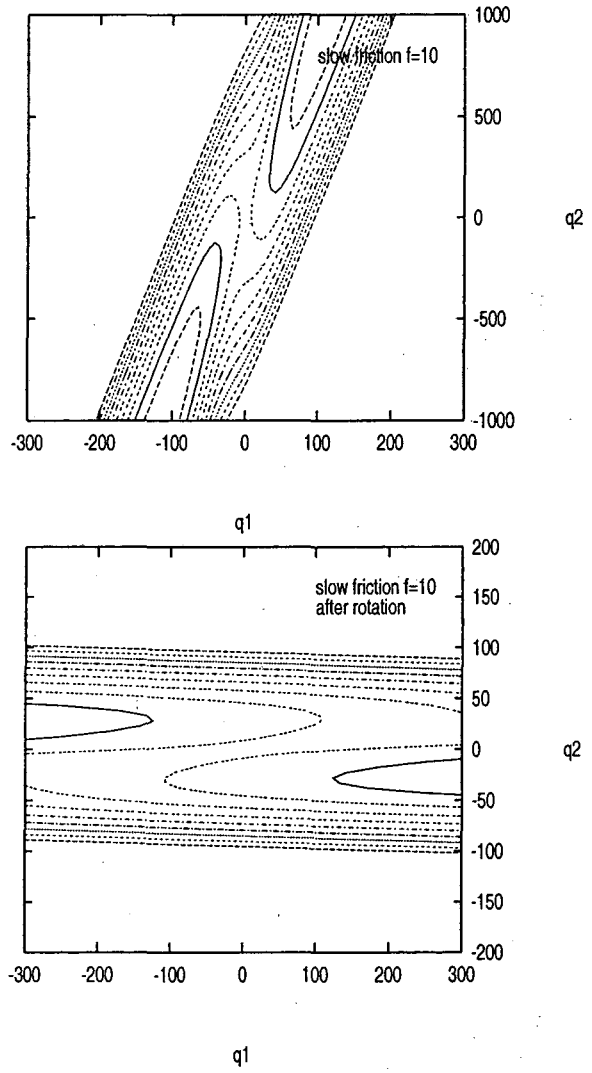

Figure 4.6: The potential energy surfaces of the two situations discussed in Fig. 4.5 for the model of slow solvent responses and $\eta = 10$. The upper one was plotted with the normal mode coordinate, which was obtained at the transition state geometry, and the lower one was obtained by rotating the normal mode coordinate 84 degrees anti-clockwise.

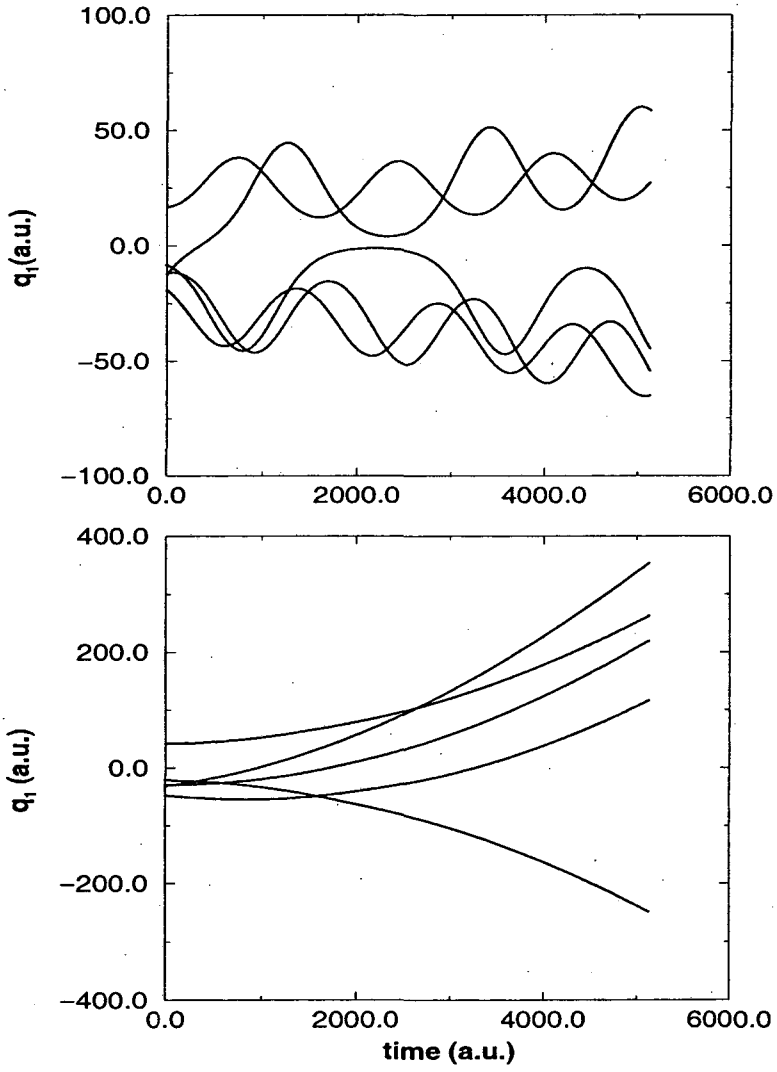

Figure 4.7: Several typical trajectories (only the reaction coordinate q_1 shown here) with the two different choices of the dividing surface in Fig. 4.6.

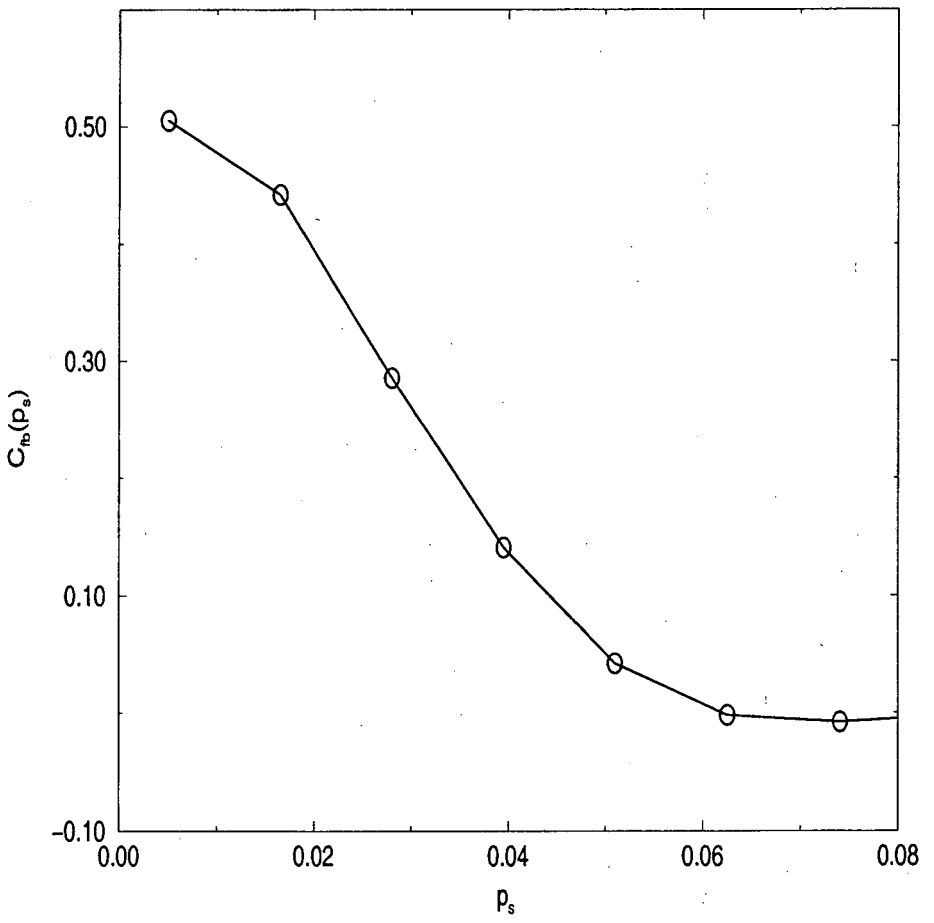

Figure 4.8: $C_{fb}(p_s)$ for the 5 medium bath mode model. The values of C_{fb} were difficult to converge at small values of p_s.

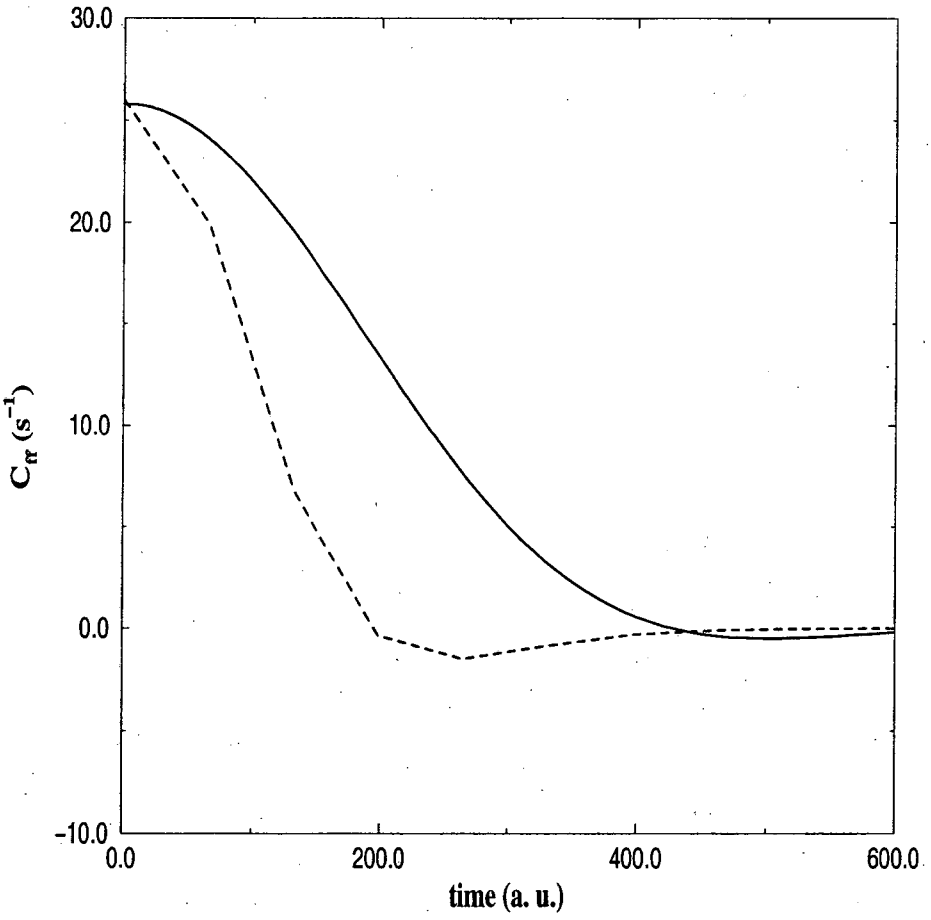

Figure 4.9: $C_{ff}(t)$ for the 1d model at 200K calculated with QM (solid line) and LSC2, respectively.

Chapter 5

Summary and Conclusions

This work has demonstrated that SC-IVR method and its approximations are capable of describing various chemical processes. These studies show that SC-IVR method is a promising candidate for studying quantum dynamic effects in large (especially condensed phase) systems. The formulation of a SC-IVR calculation is straightforward. As long as one can express the problem in a propagator form, one can readily substitute the quantum propagator by a semiclassical propagator.

A grid-based full quantum calculation scales exponentially. For large systems, the memory requirement quickly goes beyond current technology. On the other hand, a SC-IVR calculation is trajectory-based, and the memory requirement is usually just limited by what is needed for a single trajectory, which has a N^2 scaling (mostly due to the monodromy matrix). Therefore, memory requirement is usually not a concern for a SC-IVR calculation.

The bottleneck for applying the semiclassical method is efficiency. All the SC calculations end up converging a multi-dimensional complex integration, and one confronts the notorious "sign" problem. Here the "sign" problem manifests itself as the extreme difficulty to integrate a highly oscillatory function by a Monte Carlo method. In studies present in this thesis, two directions were explored to overcome the difficulty. One is to use various filtering method, and so to make the integrand less oscillatory. This direction has some success. Some calculations shown in this thesis can not be converged without the help of filtering. However,

the filtering method has its intrinsic limitations. All the filtering methods are based on analytically averaging over the vicinity of each sampling point, and thus the filtering parameter is limited to certain range so the integration is not significantly modified. The filtered integrand usually behaves better than the original one, but the "sign" problem is not fully solved. As mentioned in Chapter I, the filtering method is closely related to a renormalization procedure. Both proceed by integrating out the high-frequency part of the integrand. It remains to see if one can borrow more ideas from the renormalization group theory, which has been successfully applied in statistical mechanics.

The second direction is to work on the sampling procedure. The focus is to find a good sampling function. Some requirements of the sampling function are:
1. it should reflect the important regions of the integrand (both real and imaginary parts) as close as possible;
2. it should be easy to evaluate;
3. the normalization constant calculation should be easy.
In the studies discussed in this thesis, the modulus of the full or an approximate form of the integrand was usually chosen as the sampling function. In addition, although the integrand is generally time-dependent, a time-dependent sampling function is avoided. Considerations for this choice are to avoid propagating trajectories while evaluating the sampling function, and to treat all the time slices (or p_s grid points in a FB calculation) all in once. It is unclear if one can gain more by choosing a set of time-dependent sampling functions (the normalization constant calculation in this case might be complicated and tricky). Critical tests may be needed to solve this issue.

For very large systems, a double space or FB SC-IVR calculation may be slowed down by the monodromy matrix propagation (without it the calculation would scale linearly as a classical molecular mechanics calculation), and the prefactor calculation (which required determinant calculation of a $2F \times 2F$ matrix). Some approximate ways of calculating the prefactor were proposed in the literature, but more systematic studies are needed.

The linearized approximation in many cases gives very good results. Consider-

ing its great simplicity (not much extra cost compared to a classical calculation), more tests should be performed to examine its limitations, so one knows when the linearized result is reliable.

In conclusion, the semiclassical SC-IVR method and its approximations are promising for studying large systems, and the future focus should be on making them more efficient and practical. Applications of these methods to realistic problems are also in demand.

References

[1] (a)H.-D. Meyer and U. Manthe, Chem. Phys. bf 165, 73 (1990); (b)F. Huarte-Larranaga and U. Manthe, J. Phys. Chem. A **105**, 2522 (2001); (c)H. Wang, M. Thoss and W. H. Miller, J. Chem. Phys. **115**, 2991(2001).

[2] (a) G. Wenzel, Z. Phys. **38**, 518 (1926); (b) H. A. Kramers, Z. Phys. **39**, 828 (1926); (c) L. Brillouin, C. R. Acad. Sci. Paris **183**,24 (1926); (d) M. V. Berry and K. E. Mount, Rep. Prog. Phys. **35**, 315 (1972).

[3] M. Born. In The Mechanics of the Atom, Frederick Ungar Pub. Co., New York, 1960.

[4] I. C. Percival, Adv. Chem. Chem. **36**, 1 (1977).

[5] J. H. Van Vleck, Proc. Natl. Acad. Sci. U.S.A. **14**, 178 (1928).

[6] M. C. Gutzwiller, J. Math. Phys. **8**, 1979 (1967).

[7] C. Morette, Phys. Rev. **81**, 848 (1951).

[8] P. Choquard, Helv. Phys. Acta. **28**, 89 (1955).

[9] I. M. Gelfand and A. M. Yaglom, J. Math. Phys. **1**, 48 (1960)

[10] (a) W.H. Miller, J. Chem. Phys. **53**, 3578 (1970); for recent reviews, see ref. 16d and (b) W.H. Miller, J. Phys. Chem. A **105**, 2942 (2001).

[11] W. H. Miller, J. Chem. Phys. **62**, 1899 (1975).

[12] (a) M.F. Herman and E. Kluk, Chem. Phys. **91**, 27 (1984); (b) E. Kluk, M.F. Herman and H.L. Davis, J. Chem. Phys. **84**, 326 (1986); (c) M. F. Herman, Chem. Phys. Lett. **275**, 445 (1997); (d) B. E. Guerin and M. F. Herman, Chem. Phys. Lett. **286**, 361 (1998).

[13] (a) E.J. Heller, J. Chem. Phys. **94**, 2723 (1991); J. Chem. Phys. **95**, 9431 (1991); (b) M.A. Sepulveda and E.J. Heller, J. Chem. Phys. **101**, 8004, 8016 (1994); (c) F. Grossman and E.J. Heller, Chem. Phys. Lett. **241**, 45 (1995).

[14] K.G. Kay, J. Chem. Phys. **100**, 4377 (1994); J. Chem. Phys. **100**, 4432 (1994); J. Chem. Phys. **101**, 2250 (1994).

[15] (a) G. Campolieti and P. Brumer, Phys. Rev. A, **50**, 997 (1994); (b) D. Provost and P. Brumer, Phys. Rev. Lett. **74**, 250 (1995); (c) G. Campolieti and P. Brumer, J. Chem. Phys. **109**, 2999 (1998); (d) B.R. McQuarrie and P. Brumer, Chem. Phys. Lett. **319**, 27 (2000).

[16] (a) S. Garashchuk and D.J. Tannor, Chem. Phys. Lett. **262**, 477 (1996); (b) S. Garashchuk, F. Grossmann, and D.J. Tannor, J. Chem. Soc., Faraday Trans. **93**, 781 (1997); (c) S. Garashchuk and D.J. Tannor, J. Chem. Phys. **109**, 3028 (1998), (d) D.J. Tannor and S. Garashchuk, Ann. Rev. Phys. Chem. **51**, 553 (2000).

[17] (a) A.R. Walton and D.E. Manolopoulos, Mol. Phys. **87**, 961 (1996); (b) A.R. Walton and D.E. Manolopoulos, Chem. Phys. Lett. **244**, 448 (1995); (c) M.L. Brewer, J.S. Hulme, and D.E. Manolopoulos, J. Chem. Phys. **106**, 4832 (1997).

[18] (a) W.H. Miller, J. Chem. Phys. **95**, 9428 (1991); (b) B.W. Spath and W. H. Miller, J. Chem. Phys. **104**, 95 (1996); (c) X. Sun and W.H. Miller, J. Chem. Phys. **106**, 916 (1997); (d) X. Sun and W.H. Miller, J. Chem. Phys. **106**, 6346 (1997); (e) X. Sun and W. H. Miller J. Chem. Phys. **108**, 8870 (1998); (f) V.S. Batista, M.T. Zanni, B.J. Greenblatt, D.M. Neumark, and W.H. Miller, J. Chem. Phys. **110**, 3736 (1999); (g) V. Guallar, V.S. Batista, and W.H. Miller,

J. Chem. Phys. **110**, 9922 (1999); (h) D.E. Skinner and W.H. Miller, Chem. Phys. Lett. **300**, 20 (1999); (i) E.A. Coronado, V.S. Batista, and W.H. Miller, J. Chem. Phys. **112**, 5566 (2000); (j) M. Thoss, W.H. Miller, and G. Stock, J. Chem. Phys. **112**, 10282 (2000).

[19] J. Xing, E. A. Coronado and W. H. Miller, J. Phys. Chem. B **105** 6574 (2001).

[20] E. A. Coronado, J. Xing and W. H. Miller, Chem. Phys. Lett. **349** 521 (2001).

[21] (a) D.V. Shalashilin and B. Jackson, Chem. Phys. Lett. **291**, 143 (1998); (b) D.V. Shalashilin and B. Jackson, Chem. Phys. Lett. **318**, 305 (2000).

[22] (a) G. Stock and M. Thoss, Phys. Rev. Lett. **78**, 578 (1997); (b) M. Thoss and G. Stock, Phys. Rev. A. **59**, 64 (1999).

[23] G. van de Sand and J.-M. Rost, Phys. Rev. Lett. **83**, 524 (1999).

[24] F. Grossmann, Phys. Rev. A. **60**, 1791 (1999).

[25] H. B. Wang, X. Sun, and W. H. Miller, J. Chem. Phys. **108** 9726, 1998.

[26] (a) X. Sun, H. B. Wang, and W. H. Miller, J. Chem. Phys. **109** 4190, 1998; (b) X. Sun, H. B. Wang, and W. H. Miller, J. Chem. Phys. **109** 7064, 1998;

[27] H. Goldstein, in *Classical Mechanics* (Addison-Wesley, London, 1980).

[28] W.H. Miller, Faraday. Discuss. **110**, 1 (1998).

[29] X. Sun and W. H. Miller, J. Chem. Phys. **110**, 6635 (1999).

[30] (a) H. Wang, M. Thoss, and W. H. Miller, J. Chem. Phys. **112**, 47 (2000); (b) R. Gelabert, X. Giménez, M. Thoss, H. Wang, and W. H. Miller, J. Phys. Chem. A. **104**, 10321 (2000); (c) H. Wang, M. Thoss, K. L. Sorge, R. Gelabert, X. Giménez, and W. H. J. Chem. Phys. **114**, 2562 (2001); (d) R. Gelabert, X.

Giménez, M. Thoss, H. Wang, and W. H. Miller, J. Chem. Phys., **114**, 2572 (2001).

[31] M. Thoss, H. Wang, and W. H. Miller, J. Chem. Phys. **114**, 9220 (2001).

[32] V.S. Filinov, Nuc. Phys., B **271**, 717 (1986).

[33] H. Wang, D. E. Manolopoulos, and W. H. Miller, J. Chem. Phys. **115**, 6317 (2001).

[34] N. Makri and W.H. Miller, Chem. Phys. Lett. **139**, 10 (1987);

[35] M. F. Herman, Chem. Phys. Lett. **275**, 445 (1997).

[36] R. Kosloff, J. Phys. Chem. **92**, 2086 (1988).

[37] R. Schinke, in *Photodissociation Dynamics* (Cambridge University Press, Cambridge, 1993)

[38] D. Coker, in *Computer Simulation in Chemical Physics*, Ed. M. Allen and D. Tildesley (Kluwer Academic Publishers, Dordrecht, 1993).

[39] J. C. Tully, in *Computer Simulation in Chemical Physics*, Ed. B. Berne and D. Coker (World Scientific, Dordrecht, 1998).

[40] P. Ehrenfest, Z. Phys. **45**, 455 (1927).

[41] M. D. Hack and D. G. Truhlar, J. Chem. Phys. **104**, 7917 (2000).

[42] H. D. Meyer and W. H. Miller, J. Chem. Phys. **71**, 2156 (1979).

[43] W. H. Miller and C. W. McCurdy, J. Chem. Phys. **69**, 5163 (1978).

[44] Y. L. Volovuev, M. D. Hack, D. G. Truhlar and D. L. Thompson, J. Phys. Chem. **103**, 6225 (1999).

[45] J. Tully, J. Chem. Phys. **92**, 1061 (1990).

[46] H. Wang, X. Song, D. Chandler and W. H. Miller, J. Chem. Phys. **110**, 4828 (1999).

[47] V. S. Batista and W. H. Miller, J. Chem. Phys. **108**, 498 (1998).

[48] S. Bonella and D. Coker, preprint.

[49] D. W. Mclaughlin, J. Math. Phys. **13**, 1099 (1972).

[50] W. H. Miller and T. F. George, J. Chem. Phys. **56**, 5668 (1972).

[51] T. F. George and W. H. Miller, J. Chem. Phys. **56**, 5722 (1972).

[52] T. F. George and W. H. Miller, J. Chem. Phys. **57**, 2458 (1972).

[53] W. H. Miller, Adv. Chem. Phys. **25**, 69 (1974).

[54] R. A. Marcus and M. E. Coltrin, J. Chem. Phys. **67**, 2609 (1977).

[55] K. G. Kay, J. Chem. Phys. **103**, 2313 (1997).

[56] F. Grossmann and E. J. Heller, Chem. Phys. Lett. **241**, 45 (1995).

[57] E. J. Heller, J. Phys. Chem. A **103**, 10433 (1999).

[58] N. Makri and W. H. Miller. J. Chem. Phys. **91**, 4026 (1989).

[59] S. Keshavamurthy and W. H. Miller, Chem. Phys. Lett. **205**, 96 (1993).

[60] J. C. Tully and R. K. Preston, J. Chem. Phys. **55**, 562 (1971).

[61] T. D. Sewell, Y. Guo, and D. L. Thompson, J. Chem. Phys. **103**, 8557 (1995).

[62] Y. Guo, Y. Qin, D. C. Sorescu, and D. L. Thompson, J. Chem. Phys. **104**, 4041 (1996).

[63] Y. Guo and D. L. Thompson, J. Chem. Phys. **105**, 1070 (1996).

[64] Y. Guo and D. L. Thompson, J. Chem. Phys. **105**, 7480 (1996).

[65] Y. Guo, S. Li, and D. L. Thompson. J. Chem. Phys. **107**, 2853 (1997).

[66] Y. Guo, A. K. Wilson, C. F. Chabalowski, and D. L. Thompson. J. Chem. Phys. **109**, 9258 (1998).

[67] Y. Guo, T. D. Sewell, and D. L. Thompson. J. Phys. Chem. A **102**, 5040 (1998).

[68] S. Keshavamurthy and W. H. Miller. Chem. Phys. Lett. **218**, 189 (1994).

[69] R. Das and S. Keshavamurthy. Chem. Phys. Lett. **326**, 544 (2000).

[70] B. Spath and W. H. Miller, J. Chem. Phys. **104**, 95 (1996).

[71] W. H. Miller, J. Chem. Phys. **53**, 3578 (1970).

[72] W. H. Miller and C. W. McCurdy, J. Chem. Phys. **70**, 3177 (1979).

[73] H. D. Meyer and W. H. Miller, J. Chem. Phys. **70**, 3214 (1979).

[74] H. D. Meyer and W. H. Miller, J. Chem. Phys. **72**, 2272 (1980).

[75] C. Eckart, Phys. Rev. **35**, 1303 (1930).

[76] M. D. Feit and J. A. Fleck Jr, J. Chem. Phys. **301**, 1983 (1983).

[77] K. Takatsuka and H. Ushiyama, Phys. Rev. A **51**, 4353 (1995).

[78] H. Ushiyama and K. Takatsuka, J. Chem. Phys. **106**, 7023 (1997).

[79] K. Takatsuka, H. Ushiyama, and A Inoue-Ushiyama, Phys. Rep. **322**, 347 (1999).

[80] L. D. Landau and E. M. Lifshitz, in *Quantum Mechanics: Non-Relativistic Theory*, page 79 (Pergamon, Oxford, 1965).

[81] H. Eyring, J. Chem. Phys. **3**, 107 (1935).

[82] E. Wigner, J. Chem. Phys. **5**, 720 (1937).

[83] C. Dellago, P. Bolhuis, F. S. Csajka, and D. Chandler, J. Chem. Phys. **108**, 1964 (1998).

[84] F. J. McLafferty and P. Pechukas, Chem. Phys. Lett. **27**, 511 (1974).

[85] S. Chapman, B. C. Garrett and W. H. Miller, J. Chem. Phys. **63**, 2710 (1975).

[86] E. Pollak, J. Chem. Phys. **74**, 6765 (1981).

[87] M. J. Gillan, J. Phys. Chem. **20**, 3621 (1987).

[88] G. A. Voth, D. Chandler and W. H. Miller, J. Phys. Chem. **93**, 7009 (1989).

[89] S. C. Tucker and D. G. Truhlar, in *New Theoretical Concepts for Understanding Organic Reactions* (Kluwer, Dordrecht, 1989).

[90] E. Pollak and J. L. Liao, J. Chem. Phys. **108**, 9711 (1998).

[91] M. Sprik, M. Klein and D. Chandler, Phys. Rev. B **31**, 4234 (1985).

[92] D. T. Colbert and W. H. Miller, J. Chem. Phys. **96**, 1982 (1992).

[93] (a) W.H. Miller, J. Chem. Phys. **61**, 1823 (1974); (b) W.H. Miller, S.D. Schwartz and J.W. Tromp, J. Chem. Phys. **79**, 4889 (1983).

[94] See also, T. Yamamoto, J. Chem. Phys. **33**, 281 (1960).

[95] T. Yamamoto, H. Wang, and W. H. Miller, J. Chem. Phys. **116**, 7335 (2002).

[96] R. P. McRae, G. K. Schenter, B. C. Garrett, G. R. Haynes, G. A. Voth, and G. C. Schatz, J. Chem. Phys. **97**, 7392 (1992).

[97] J. L. Liao and E. Pollak, J. Chem. Phys. **110**, 80 (1999).

[98] N. Metropolis, A. W. Rosenbluth, M. N. Rosenbluth, H. Teller, and E. Teller, J. Chem. Phys. **21**, 1087 (1953).

[99] M. P. Allen, and D. J. Tildesley, in *Computer Simulation of Liquids* (Oxford University Press, Oxford, 1987).

[100] H. B. Wang, and W. H. Miller, Chem. Phys. Lett. **307**, 463 (1999).

ERNEST ORLANDO LAWRENCE BERKELEY NATIONAL LABORATORY
ONE CYCLOTRON ROAD | BERKELEY, CALIFORNIA 94720

Prepared for the U.S. Department of Energy under Contract No. DE-AC03-76SF00098